Evaluation of 3D Subgrid-Scale Fluxes in Kilometer-Scale Simulations of an Idealized Squall Line

Shiwei Sun,[a,b] Kefeng Zhu,[a,b] Bowen Zhou,[c] and Ming Xue[d]

[a] *Nanjing Innovation Institute for Atmospheric Sciences, Chinese Academy of Meteorological Sciences-Jiangsu Meteorological Service, Nanjing, China*
[b] *Jiangsu Key Laboratory of Severe Storm Disaster Risk, Key Laboratory of Transportation Meteorology of CMA, Nanjing, China*
[c] *State Key Laboratory of Severe Weather Meteorological Science and Technology, NJU and School of Atmospheric Sciences, Nanjing University, Nanjing, China*
[d] *Center for Analysis and Prediction of Storms, University of Oklahoma, Norman, Oklahoma*

(Manuscript received 2 June 2024, in final form 25 June 2025, accepted 10 July 2025)

ABSTRACT: Subgrid-scale (SGS) turbulent mixing is essential to convection-permitting simulations where turbulent fluxes are partially resolved and partially subgrid scale. This study investigates the characteristics of the three-dimensional (3D) SGS fluxes of an idealized squall line in a weak sheared environment. The 3D SGS fluxes on kilometer-scale grids are obtained by coarse graining a benchmark large-eddy simulation (LES) conducted with the Advanced Regional Prediction System model. Countergradient (CG) transport is found in both horizontal and vertical SGS fluxes in the updraft region, which results from nonlocal transport associated with the tilted updraft. Using moist-conserved variables for the identification of CG fluxes, the spatial distribution and the occurrence rates of the CG and the downgradient fluxes are investigated. A scale-similarity (Hgrad) and a conventional gradient-diffusion [turbulence kinetic energy (TKE)] SGS closures are then evaluated at kilometer-scale resolutions against the LES. Both the offline evaluation and the online simulations demonstrate improvements of the Hgrad closure over the TKE closure, mostly due to the former's ability to represent CG fluxes. Through sensitivity experiments, we investigate the role of horizontal flux parameterization in predicting the structure and intensity of deep convection with tilted updraft.

SIGNIFICANCE STATEMENT: Current-day numerical weather prediction models operate on kilometer-scale grids that permit partially explicit resolution of deep convection. Accurate parameterization of the unresolved subgrid-scale (SGS) turbulence is key to improving kilometer-scale simulations of deep convection. Former studies on SGS turbulence for kilometer-scale grids are often based on upright deep convection and point to the essential role of vertical SGS flux parameterization. We investigate a vertically tilted deep convective system under the influence of the cold pool. Our findings show that the contribution of the horizontal SGS fluxes may be comparable to the vertical SGS fluxes in kilometer-scale simulations of convective storms with tilted structures.

KEYWORDS: Subgrid-scale processes; Turbulence; Squall lines; Shear structure/flows; Large eddy simulations; Mesoscale models

1. Introduction

Kilometer-scale numerical weather prediction (NWP) models are operational in weather centers worldwide (see Benjamin et al. 2018, and references therein). Their performances have also been studied for more than two decades (e.g., Weisman et al. 1997; Bryan et al. 2003; Warner and Hsu 2000; Kain2004; Liu et al. 2001; Wyngaard 2004; Honnert et al. 2011). At kilometer-scale resolutions,[1] NWP models begin to resolve convective storms explicitly and are called convection-permitting models (CPMs; Schwartz et al. 2009; Prein et al. 2015; Langhans et al. 2012; Clark et al. 2016) to differentiate from traditional mesoscale models where the representation of deep moist convection relies on cumulus parameterization. As the spatial scale of convective clouds is usually on the order of 1–10 km (Emanuel 1994; Houze 1993), the extent of their resolution by CPMs is best described as partly resolved and partly subgrid-scale (Bryan et al. 2003; Arakawa and Wu 2013).

In operational practice, deep cumulus parameterizations are often turned off in CPMs, as the predictions of deep convection and the associated precipitation generally improve without cumulus parameterization (Xue et al. 2003; Lean et al. 2008; Pearson et al. 2010; Zhu et al. 2018). However, many studies have also shown that only a portion of the in-cloud turbulent motions are explicitly resolved at such borderline resolutions (Weisman et al. 1997; Bryan et al. 2003; Arakawa and Wu 2013; Lebo and Morrison 2015; Shi et al. 2019; Tang and Kirshbaum 2020; Ye et al. 2023). More specifically, the resolved motions are mostly those associated with the broader convective core updrafts, whereas the smaller turbulent eddies that are either embedded in or at the periphery of the updrafts are poorly resolved (Sun et al. 2021, hereafter S21; Liu and Zhou 2022).

---

[1] In this study, we loosely refer to "kilometer-scale resolutions" as the resolution range between several hectometers and several kilometers.

Corresponding author: Kefeng Zhu, zhukf@cma.gov.cn

DOI: 10.1175/MWR-D-24-0109.1

Contributions from these unresolved eddies could account for a significant portion of the overall turbulent transport. Without proper parameterization of their effects on the resolved flow, convective storms simulated by CPMs are often too wide and too energetic (Fan et al. 2017; Kendon et al. 2021). Some are subjected to various structural and location errors (Fiori et al. 2010; Lebo and Morrison 2015; Prein et al. 2015; Clark et al. 2016), and some are biased toward frequent light scattered precipitation (Xue et al. 2013; Clark et al. 2016).

To represent the effects of in-cloud SGS turbulent eddies in deep convection, a number of studies attempted to extend conventional turbulence closures that are originally designed for large-eddy simulations (LESs) on $\mathcal{O}(10–100)$ m grids to CPMs. The adapted turbulence closures are mostly gradient-diffusion schemes, where the parameterized flux of a variable φ points to its downgradient direction. Typical examples include the three-dimensional (3D) Smagorinsky (1963) and the 1.5-order turbulence kinetic energy (TKE; Moeng 1984) closures. Their adaptation to kilometer-scale grids focuses mostly on tuning model coefficients to improve a certain aspect of the storm simulation. For example, Takemi and Rotunno (2003) increased the turbulent mixing coefficients in the Smagorinsky and the TKE closures to suppress numerical noises in kilometer-scale squall-line simulations. Zhang et al. (2018) adjusted the horizontal diffusion coefficients in simulations of tropical cyclones (TCs) and improved the forecasts of TC strength, radius of maximum wind, and boundary layer height. Zhang et al. (2021) tuned the Smagorinsky coefficient to improve storm precipitation forecasts.

However, LES models are designed to parameterize only local turbulent transport, allowing nonlocal transport to be explicitly resolved. In deep convection, the latter is associated with organized convective updrafts that are capable of transporting a variable *up* its local gradient, producing the so-called countergradient (CG) fluxes (Deardorff 1966). A typical example is the upward transport of sensible heat in convective updrafts against the local stratification. In the hydrostatic limit with coarse resolutions, all of the CG fluxes are of subgrid scale, requiring SGS schemes to be capable of handling CG vertical transport (e.g., Holtslag and Moeng 1991; Siebesma et al. 2007). At convection-permitting resolutions, the resolved flow is able to capture some but not all CG transport associated with the nonlocal eddies due to the borderline resolution as previously mentioned. The remainder is of subgrid scale and must be parameterized.

The presence countergradient SGS fluxes have been reported in several kilometer-scale simulation studies of mesoscale convective systems (Verrelle et al. 2017; Strauss et al. 2019), supercells (S21), and TCs (Shi and Wang 2022; Ye et al. 2023). Most of these studies focus on the *vertical* CG fluxes, while their *horizontal* counterparts are seldom investigated. Part of the reason, we suspect, is that the tropical deep convections chosen in these aforementioned studies have mostly upright updrafts, leading to significant vertical CG fluxes. However, when vertical flux $\overline{w'c'}$ associated with a convective updraft is tilted by the vertical wind shear $\partial_z\overline{u}$ and/or the cold pool, horizontal flux $\overline{u'c'}$ is created through the action of the mean-gradient production term $\overline{w'c'}\partial_z\overline{u}$ [Wyngaard 2004; Eq. (18)] and could be pointed up the horizontal gradient of $\overline{c}$ ($\partial_x\overline{c}$) as evidenced in S21 and Ye et al. (2023). In this work, we simulate an idealized squall line where convective updrafts are tilted upshear with the Advanced Regional Prediction System (ARPS; Xue et al. 2000, 2001) model and investigate countergradient SGS fluxes in both vertical and horizontal directions.

The ability to represent countergradient SGS fluxes is of primary importance to CPM simulations of deep convection (Shi et al. 2019 and references therein). This is, however, a challenging task for gradient-diffusion-type LES closures which are limited to the parameterization of downgradient fluxes. The proper representation of countergradient SGS fluxes requires a paradigm shift away from the conventional gradient-diffusion framework. One promising model, originally developed as an LES closure by Clark et al. (1977), was adapted to the kilometer-scale simulations of deep moist convection by Moeng et al. (2010). It is a nonlinear-scale-similarity closure that is capable of representing countergradient SGS fluxes (see section 2a for details). Follow-up studies have shown that the Clark model outperforms gradient-diffusion closures in the representation of storm structure and precipitation at kilometer-scale resolutions (Verrelle et al. 2017; Hanley et al. 2019; Strauss et al. 2019; S21; Ye et al. 2023), although most of these studies apply the model to the vertical fluxes only. Our study adopts the Clark model for both the horizontal and the vertical fluxes and evaluates its performance with an emphasis on the representation of CG fluxes.

2. Data and methods

a. Turbulence closures

The 1.5-order TKE and the nonlinear Clark closures are used in this work. The former is a widely used LES closure developed by Deardorff (1980) and Moeng (1984), where the SGS momentum and scalar fluxes are parameterized as

$$\tau_{ij} \equiv \widetilde{u_i u_j} - \tilde{u}_i\tilde{u}_j = -K_M\left(\frac{\partial \tilde{u}_i}{\partial x_j} + \frac{\partial \tilde{u}_j}{\partial x_i}\right),$$

$$\tau_{ci} \equiv \widetilde{u_i c} - \tilde{u}_i\tilde{c} = -K_H\frac{\partial \tilde{c}}{\partial x_i}. \qquad (1)$$

The overtilde is a spatial filter operator, u_i represents the ith component of the wind vector, and c represents a generic scalar such as potential temperature θ or the water vapor mixing ratio q_v. In Eq. (1),

$$K_M = C_k\sqrt{e}l, \quad K_H = \frac{K_M}{\mathrm{Pr}_T}, \qquad (2)$$

are the eddy viscosity and diffusivity, where the subscripts M and H stand for momentum and heat, respectively. The $C_k = 0.1$ is a model constant; e is the subgrid TKE; and l is a turbulence length scale, which can be separately prescribed for the horizontal l_h and the vertical l_v directions. In the ARPS model, l is set based on the grid aspect ratio. On near-isotropic grids ($\Delta x, \Delta y \approx \Delta z$), a single length $l_h = l_v = (\Delta x\Delta y\Delta z)^{1/3}$ is adopted. On anisotropic grids ($\Delta x, \Delta y \gg \Delta z$) which applies to CPMs, $l_h = (\Delta x \Delta y)^{1/2}$ and $l_v = \Delta z$ are parameterized differently. Under stably stratified conditions, l is further constrained by the buoyancy length scale $0.76\sqrt{e}/N$, where N is the Brunt–Väisälä frequency. The Pr_T is the turbulent Prandtl number and is set to $1/(1 + 2l_v/\Delta z)$ (Moeng 1984). In this study, the 1.5-order TKE closure is applied to both the LES and the kilometer-scale simulations using the isotropic and the anisotropic length scales, respectively.

The second closure to be evaluated was proposed by Clark et al. (1977, 1979) for LES. It was introduced to CPMs by Moeng et al. (2010) and Moeng (2014). The scalar SGS flux is parameterized as

$$\tau_{ci} \equiv \widetilde{u_i c} - \widetilde{u}_i \widetilde{c} = C_s \frac{\Delta^2}{12}\left(\frac{\partial \widetilde{u}_i}{\partial x}\frac{\partial \widetilde{c}}{\partial x} + \frac{\partial \widetilde{u}_i}{\partial y}\frac{\partial \widetilde{c}}{\partial y}\right), \tag{3}$$

where C_s is a model constant and $\Delta = (\Delta x \Delta y)^{1/2}$ is the horizontal grid spacing. Equation (3) can be formally obtained by reconstructing (or deconvoluting) the unfiltered variable through Taylor series expansion [see the appendix of Moeng et al. (2010) for details]. Since the *horizontal gradients* of the resolved variables are used to parameterize the SGS fluxes in Eq. (3), it is also referred to as the Hgrad closure by Verrelle et al. (2017). For kilometer-scale storm simulations, S21 proposed the following scale-dependent model coefficients for the vertical and the horizontal fluxes separately:

$$\begin{aligned} C_{s,\mathrm{v}}(\Delta) &= 0.074\Delta^{0.63}, \\ C_{s,\mathrm{h}}(\Delta) &= 0.27\Delta^{0.41}. \end{aligned} \tag{4}$$

These grid-dependent coefficients are used for all simulations in this study. In S21, it was found that the Hgrad closure applied to the momentum fluxes would lead to numerical instability. Therefore, we only use the Hgrad closure for the scalar fluxes and resort to the TKE closure for momentum fluxes.

b. Numerical setup

Numerical setup for the idealized squall line follows Bryan et al. (2003). Specifically, the initial temperature and moisture profiles are from Weisman and Klemp (1982), which are associated with a high convective available potential energy (CAPE) value of about 2400 J kg^{-1}. The initial wind profile is from Weisman et al. (1997), where westerly winds increase from 0 at the surface to 10 m s^{-1} at 2.5-km height and remain constant above. Similar wind profiles have also been used for tropical squall lines (e.g., Trier et al. 1996; Lafore and Moncrieff 1989). To keep the squall line near the center of the simulation domain, a Galilean shift was applied with 18.0 m s^{-1} winds subtracted from each level. The squall line is initiated by a north–south line thermal with a maximum amplitude of 2 K. The thermal is centered at the ground level and has a vertical height of 1.5 km and a horizontal radius of 10 km. Random perturbations with an amplitude of 0.2 K are introduced to the center 1/3 of the thermal at the ground level to speed up the development of turbulence.

Numerical simulations are conducted by version 5.3.4 of the ARPS model. The LES uses 50-m uniform horizontal grid spacing, while the vertical spacing is stretched from 20 m near the ground to 400 m at the domain top. The numerical domain consists of 3960 × 1200 × 90 grid points. It is 298 km in the east–west cross-line (x) direction, 60 km in the north–south along-line (y) direction, and 18 km in height. The cross-line lateral boundaries are open radiative, and the along-line boundaries are periodic. Free-slip conditions are specified at the bottom boundary, and there are no surface sensible or latent heat fluxes. Such bottom boundary condition is widely adopted in previous studies, so that the squall line is only driven by CAPE and vertical wind shear (Weisman et al. 1997; Takemi and Rotunno 2003; Bryan et al. 2003; Morrison et al. 2009; Lebo and Morrison 2015; Jensen et al. 2018). The Coriolis factor is set to 0 to represent a tropical environment. The single-moment Lin scheme (Lin et al. 1983) and the 1.5-order TKE closure with isotropic length scale are used for microphysics and SGS turbulence, respectively. The simulations use the fourth-order advection for both momentum and scalars, with Zalesak (1979)'s flux-corrected transport applied to scalar advection. Fourth-order computational mixing with a coefficient of 5×10^{-4} s^{-1} is also applied to suppress grid-scale noises. The time step is 0.1 s, and the model is run for 4 h to obtain a mature and quasi-steady-state squall line. The outputs are saved at every 10 min for the analysis.

For the CPM simulations conducted at 250-m, 500-m, 1-km, 2-km, and 4-km horizontal grid spacings, the numerical domain is enlarged to 320 km × 120 km × 18 km. The same vertical grid configuration as the LES is adopted to focus on the effect of the horizontal grid. The model time steps are set to 0.2, 1, 2, 4, and 4 s for the five grid resolutions, respectively, and the numerical mixing coefficients are modified to 5×10^{-4}, 5×10^{-4}, 1×10^{-3}, 1.5×10^{-3}, and 2×10^{-3} s^{-1} to reduce the numerical errors in the moist absolutely unstable layer (MAUL) when the horizontal grid spacing is over 1 km (Bryan 2005). The numerical setup and the initial condition for these runs are the same as that used for the LES, except for the turbulence closure. To pin down the relative importance of vertical and horizontal flux parameterizations, we apply the TKE closure (with the anisotropic option) and the Hgrad closure individually to the horizontal and the vertical fluxes, resulting in four closure combinations for each resolution. The naming conventions are based on the turbulence closures used. For example, the hHgrad_vTKE run uses the Hgrad closure for the horizontal and the TKE closure for the vertical SGS flux, hence the small letter "h"[2] and "v" in front of the closure names.

c. Filtering LES data

The LES outputs are coarse grained to 250-m, 500-m, 1-km, 2-km, and 4-km grid spacings to obtain benchmark solutions for the corresponding resolution. Coarse-graining is conducted with a 2D Gaussian filter following Moeng et al.

---

[2] The 'h' is not to be confused with the capital letter 'H' in Hgrad. The h denotes the horizontal *flux*, while H is for the horizontal *gradient* used in the closure in Eq. (3).

(2010). For a generic variable ϕ, the filtered variable is obtained by

$$\widetilde{\phi}(x, y) = \iint \phi G(x - \eta, y - \zeta) d\eta d\zeta, \tag{5}$$

where η and ζ are the dummy variables for the integration and G is the 2D Gaussian kernel defined as

$$G(x - \eta, y - \zeta) = \frac{6}{\pi}\frac{1}{\Delta^2}\exp\left\{-\frac{6[(x-\eta)^2 + (y-\zeta)^2]}{\Delta^2}\right\}, \tag{6}$$

and Δ is both the filter width and the target grid spacing. The filtered SGS fluxes $\tau^{\mathrm{SGS}}_{\phi i}$ are obtained by

$$\tau^{\mathrm{SGS}}_{\phi i} = \widetilde{\phi u_i} - \widetilde{\phi}\widetilde{u}_i. \tag{7}$$

Note that the SGS fluxes on the original LES grids are ignored due to their small contributions (less than 10%).

To assess the relative contribution of the SGS fluxes on kilometer-scale grids, the total fluxes are needed. This is a nontrivial task for storms, due to difficulties in obtaining an objective reference state $\overline{\varphi}$, based on which the perturbations $\varphi' = \varphi - \overline{\varphi}$ are computed. Under horizontally homogenous conditions, such as in dry convective boundary layer, $\overline{\varphi}$ is well defined by the horizontal average (Sullivan and Patton 2011). However, in a convective storm characterized by spatial heterogeneity, the horizontal average is no longer an appropriate representation of the background state. The same issue arises for the identification of CG fluxes where the gradient of $\overline{\varphi}$ is required. In this case, $\overline{\varphi}$ is better defined within a local area surrounding the convective updrafts rather than the domain-averaged value. In practice, the reference state is often obtained through *local* averaging, with an averaging area large enough to include the largest turbulent eddies but not too large to be affected by heterogeneity of the mesoscale flow (e.g., Green and Zhang 2015). The choice of the averaging area, or equivalently the local filter width, is, however, subjective due to the lack of scale separation between turbulence and mesoscale motions.

Fortunately, the difficulty with the reference state is greatly ameliorated with the quasi-2D squall-line setup, in which the along-line direction is homogeneous under the periodic boundary condition. The along-line averaging operator defined as $\langle\phi\rangle(x, z) = (1/L_y)\int \phi(x, y, z)dy$ is employed to obtain an objective reference state consisting only of the mesoscale flow. The total turbulent flux is computed as

$$\begin{aligned}\tau^{T}_{\phi i} &= \langle(\phi - \langle\phi\rangle) \times (u_i - \langle u_i\rangle)\rangle \\ &= \langle\phi u_i\rangle - \langle\phi\rangle\langle u_i\rangle,\end{aligned} \tag{8}$$

while the resolved turbulent flux on kilometer-scale grid is

$$\tau^{R}_{\phi i} = \langle(\widetilde{\phi} - \langle\phi\rangle) \times (\widetilde{u}_i - \langle u_i\rangle)\rangle. \tag{9}$$

Based on Eqs. (8) and (9), the SGS turbulent fluxes may also be computed as $\tau^{T}_{\phi i} - \tau^{R}_{\phi i}$. Note that the difference between total and the resolved fluxes is not exactly equal to $\tau^{\mathrm{SGS}}_{\phi i}$ computed based on Eq. (7) because $\langle\cdot\rangle$ is a 1D averaging operator, while $\widetilde{\cdot}$ is a 2D filter. However, the SGS fluxes obtained by both methods are in fact very close. We follow the definition of $\tau^{\mathrm{SGS}}_{\phi i}$ and use Eq. (7) to compute the benchmark SGS fluxes.

3. Benchmark LES results

In this section, data from the last hour of the 50-m LES, when the simulated squall line is at quasi-steady state, are used for the analysis. A system-relative x coordinate is adopted where the origin is placed at the front of the cold pool, defined by a −4 K surface potential temperature perturbation θ' from the inflow. Movement of the squall line is removed from the wind vectors to obtain system-relative wind fields. Time and along-line averaging are performed for the system-relative fields to obtain statistics.

a. *Overall depiction of the squall line*

In the LES, moist convection is initiated by the surface thermal and starts to generate precipitation about 30 min into the simulation. Afterward, temperature at lower levels decreases due to evaporative cooling, and a cold pool is soon established. The surface cold air spreads out in a nonsymmetric fashion as a result of the environmental eastward wind shear. The eastward-moving current is deeper and moves more slowly against incoming winds. Under favorable wind shear, the cold pool raises the inflow at its edge and sustains the convection as predicted by the Rotunno–Klemp–Weisman (RKW) theory (Rotunno et al. 1988; Weisman et al. 1988; Weisman and Rotunno 2004). In the squall-line reference system, the east and the west directions are referred to as the front and the rear, respectively.

Time- and along-line-averaged 2D squall-line structures are shown in Fig. 1. The mean updraft, as outlined by the black contours in all four subplots, shows a tilt over 60° from the vertical direction. Equivalent potential temperature θ_e and total water content q_t on the left panel are used for the analysis of thermodynamic and the moisture fields. They exhibit better conservation properties than θ and q_v for moist convection, as the latter does not account for phase transition. The vertical velocity w and the LES-resolved TKE [i.e., $\langle(1/2)\sum_{i=1}^{3}(u_i - \langle u_i\rangle)^2\rangle$] on the right panel are plotted to represent the dynamic and the turbulent fields.

As shown in Fig. 1a, the low-level inflow ahead of the squall line is associated with high θ_e. The high-θ_e stream extends rearward along the tilted ascending inflow. The surface region left of the origin below the tilted updraft is the cold pool. Two local maxima are found in the line-averaged w presented in Fig. 1b. One is located above the leading edge of the cold pool at around 2 km above ground level (AGL) and is associated with the dynamic lifting of the inflow. The other is located in-between the mid–upper levels and is mainly related to buoyancy. Figure 1c presents the distribution of q_t that mostly decreases with height. The high value region along the inflow is due to the transport of the water vapor by the tilted updraft. The high q_t within the cold pool is attributed to precipitation. The resolved TKE shown in Fig. 1d has large values centered above 8 km AGL, which is related to the upper part

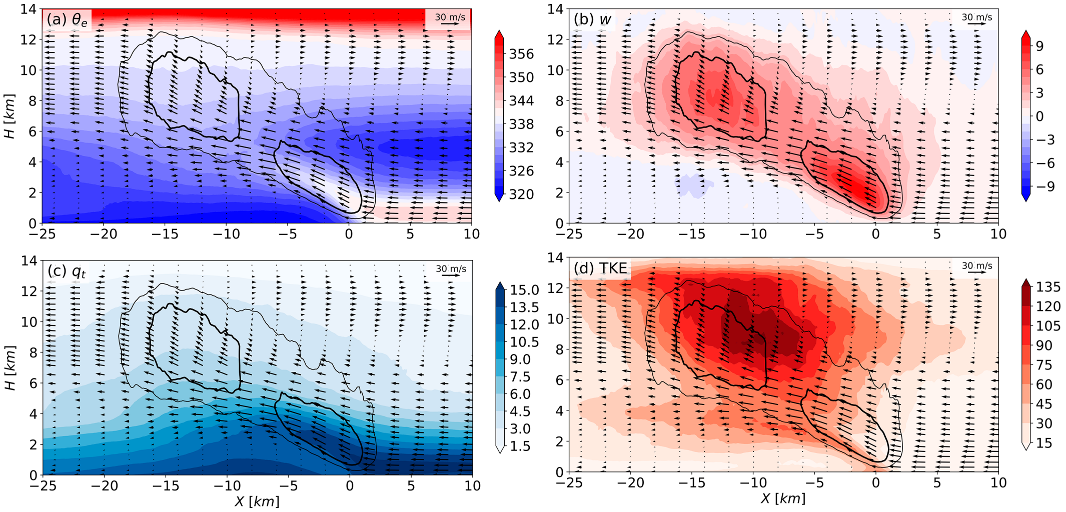

FIG. 1. Time- and along-line-averaged (a) equivalent potential temperature $\langle\theta_e\rangle$ (K), (b) vertical velocity $\langle w\rangle$ (m s^{-1}), (c) total water content $\langle q_t\rangle$ (g kg^{-1}), and (d) resolved TKE (m^2 s^{-2}) from the LES. Black contours outline the updraft core with the thin line representing $\langle w\rangle \geq 2.5$ m s^{-1} and the bold line for $\langle w\rangle \geq 5$ m s^{-1}.

of the squall-line convection, and has a secondary maximum at the interface between the cold pool and the inflow updrafts.

b. Benchmark SGS fluxes

The original LES outputs are filtered following Eqs. (7)–(9) to obtain the benchmark fluxes at kilometer-scale resolutions. The behaviors of SGS fluxes at $\Delta = 1$ km are presented and analyzed. SGS fluxes obtained at other kilometer-scale filter widths yield similar results and are not shown. The time- and along-line-averaged total turbulent heat fluxes $\tau^T_{\theta_e i}$, along with its resolved $\tau^R_{\theta_e i}$ and SGS $\tau^{\mathrm{SGS}}_{\theta_e i}$ components, are shown in Fig. 2. The SGS ratios $\tau^{\mathrm{SGS}}_{\theta_e i}/\tau^T_{\theta_e i}$ are presented in the bottom panel. In the top panel, the total vertical heat flux $\tau^T_{\theta_e 3}$ and horizontal heat flux $\tau^T_{\theta_e 1}$ are primarily directed upward and rearward. Together, the flux vector is approximately aligned with the tilted updraft. The spatial distributions of the horizontal and vertical fluxes differ. Large upward $\tau^T_{\theta_e 3}$ are centered around 5 km AGL, just above the maximum w, while a secondary maximum is found along the leading edge of the cold pool below 2 km AGL. For the horizontal flux, the strongest front-to-rear $\tau^T_{\theta_e 1}$ is concentrated along the leading edge of the cold pool where very strong horizontal gradient of $\widetilde{\theta}_e$ exists due to the presence of the cold pool (see Fig. 1a). Above the cold pool edge, rearward transport by $\tau^T_{\theta_e 1}$ is still significant but not as strong. Above 8 km, $\tau^T_{\theta_e 1}$ flips sign due to the overturning flow.

The spatial distributions of the resolved (second row) and SGS fluxes (third row) largely resemble their respective total fluxes. The magnitude of the SGS fluxes is smaller than their resolved counterparts (note the differences in the color bars). The SGS ratio of the vertical flux is generally above 20% in the updraft region and is close to 40% in the updraft core as shown in Fig. 2g. For the horizontal flux, the SGS component contributes to over 30% of the total flux along the inflow above the leading edge of the cold pool as shown in Fig. 2h. Higher up, the horizontal SGS flux ratio drops, and SGS contribution is no longer significant above 5-km height. Figures 2g and 2h together indicate nonnegligible contributions of *both vertical and horizontal* SGS fluxes at 1-km grid spacing. Within the updraft core, the SGS contribution may even be comparable to that of the resolved flow.

As shown in Fig. 2, the SGS and total fluxes ($\tau^{\mathrm{SGS}}_{\phi i}$ and $\tau^T_{\phi i}$) are generally aligned in the same direction in the convective region. Spatial averaging within -20 km $< x < 5$ km yields vertical profiles of the SGS fluxes $\tau^{\mathrm{SGS}}_{\phi i}$ at different resolutions and their relative contributions to the total turbulent fluxes in the convective region, as shown in Fig. 3. For the vertical heat flux $\tau_{\theta_e 3}$, the convective region exhibits overall positive values (indicating upward transport), with a peak centered approximately 5 km AGL (Fig. 3a). The SGS to total flux ratio $\tau^{\mathrm{SGS}}_{\theta_e 3}/\tau^T_{\theta_e 3}$ reaches nearly 100% at ground level up to 2 km AGL at 4-km resolution and is about 75% above (Fig. 3e). Within the resolution range between 2 km and 250 m, the ratio varies from 50% to 10%. The horizontal flux $\tau^{\mathrm{SGS}}_{\theta_e 1}$ is directed rearward below 8 km AGL (Fig. 3b) and reverses direction between 8 and 12 km due to the overturning flow. The ratio $\tau^{\mathrm{SGS}}_{\theta_e 1}/\tau^T_{\theta_e 1}$ in Fig. 3f is generally lower than that of the vertical component, which is about 20% at $\Delta = 1$ km and 10% at 500 m.

In the vertical direction, the SGS flux of total water $\tau^{\mathrm{SGS}}_{q_t 3}$ is predominantly upward, and its value in the upper part of the storm (above 8 km AGL) is higher than that near the ground as shown in Fig. 3c. The ratio $\tau^{\mathrm{SGS}}_{q_t 3}/\tau^T_{q_t 3}$ in Fig. 3g is only slightly smaller than that of θ_e. The horizontal flux $\tau^{\mathrm{SGS}}_{q_t 1}$ is directed rearward at all heights below 14 km as shown in Fig. 3d. The total flux $\tau^T_{q_t 1}$ shows significant peaks at 7 and 2 km AGL, which are not evident in the SGS flux $\tau^{\mathrm{SGS}}_{q_t 1}$ at coarser resolutions. The proportion of SGS flux to total flux $\tau^{\mathrm{SGS}}_{q_t 1}/\tau^T_{q_t 1}$ is lower compared to that of θ_e, only reaching about 50% at $\Delta = 4$ km. Overall, when the horizontal grid spacing is

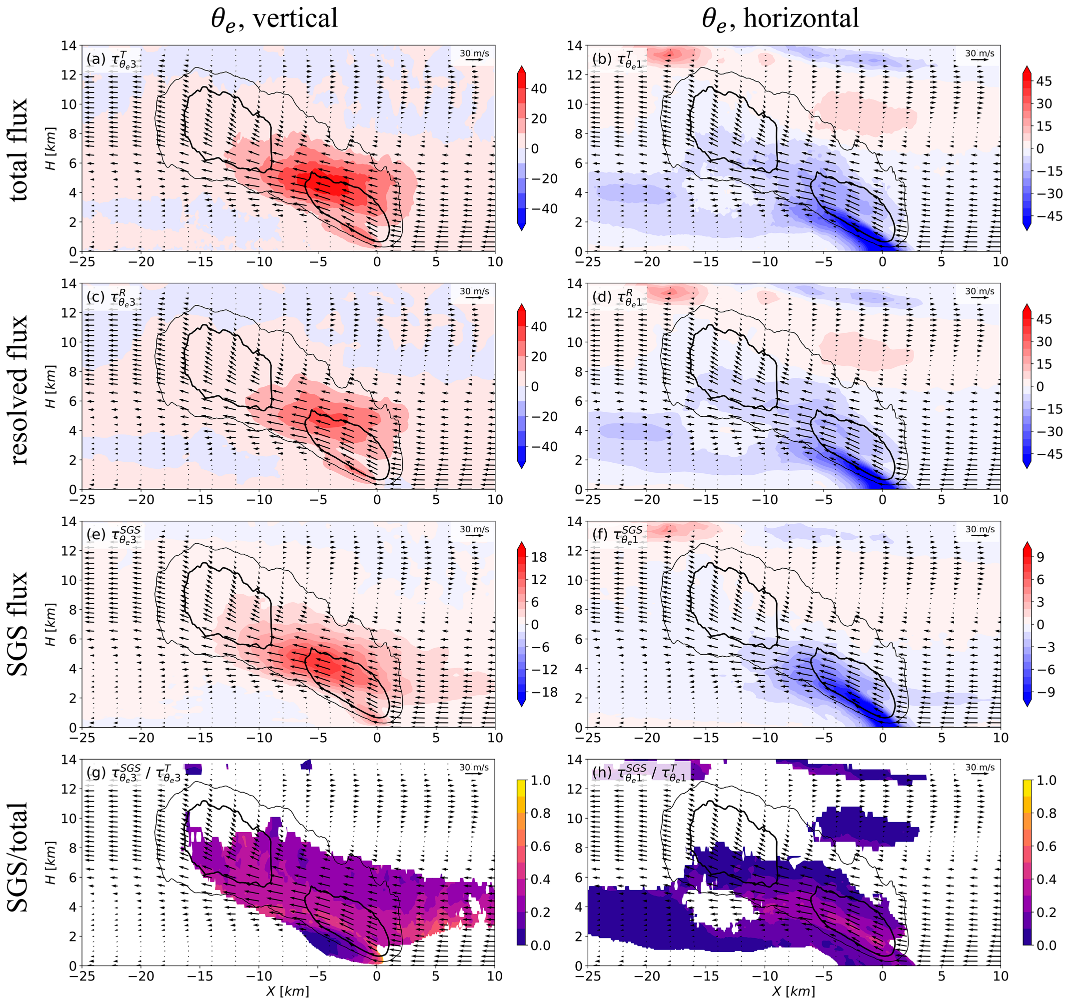

FIG. 2. Time- and along-line-averaged cross sections of (a),(b) the total, (c),(d) the resolved, (e),(f) the SGS turbulent fluxes, and (g),(h) the ratio of SGS over total flux. (left) The vertical and (right) the horizontal fluxes of θ_e filtered to 1-km spacing. Regions with τ^T being less than 10% of its maximum are masked in (g) and (h) to focus on regions with relatively large fluxes. The color scales are in units of kelvin meters per second, and note the changes of color scale in (e) and (f).

between 500 m and 4 km, the contribution of SGS flux to the total flux increases approximately from 10% to 80%, indicating that this resolution range falls in the gray zone of the simulated squall line.

Next, we focus on the SGS fluxes shown in Figs. 2e and 2f. Their downgradient (DG) and CG contributions are separately investigated. This is done by calculating the product of $\tau_{\phi i}^{\mathrm{SGS}}$ and $\partial\widetilde{\phi}/\partial x_i$ on the filtered grid (in this case, 1 km × 1 km) at every vertical level. DG and CG fluxes are identified by negative and positive product values, respectively. Again, we note that the identification of CG and DG fluxes are subjected to complications arising from the reference state and the grid spacing, as elaborated in section 2c. While the analysis produces relatively objective results thanks to the quasi-2D squall-line structure, its extension to other heterogenous convective storms should be exercised with caution.

Time- and along-line-averaged DG and CG fluxes of θ_e are shown in the first and the third rows of Fig. 4, respectively. Note that conditional averaging is performed by summing all DG and CG grid points in the along-line direction and divided by the total along-line grid points N_y, such that the averaged DG and CG fluxes directly add up to the total SGS flux in Fig. 2. Furthermore, the percentage occurrence of CG fluxes is quantified in the rightmost column of Fig. 4 as $N^{\mathrm{CG}}/N^{\mathrm{ALL}}$, where N^{CG} and N^{DG} refer to the number of CG and DG flux points and $N^{\mathrm{ALL}} = N^{\mathrm{CG}} + N^{\mathrm{DG}}$. Note that a lower threshold value of 0.5 K m s^{-1} is placed on the absolute SGS flux values to eliminate very small SGS fluxes that may be associated with numerical noises. Besides the θ_e fluxes, we also include fluxes of θ for comparison. This is because many NWP models such as the Weather Research and Forecasting (WRF) Model (Skamarock et al. 2021), the Model for Prediction Across Scales (MPAS; Skamarock et al. 2012), and ARPS

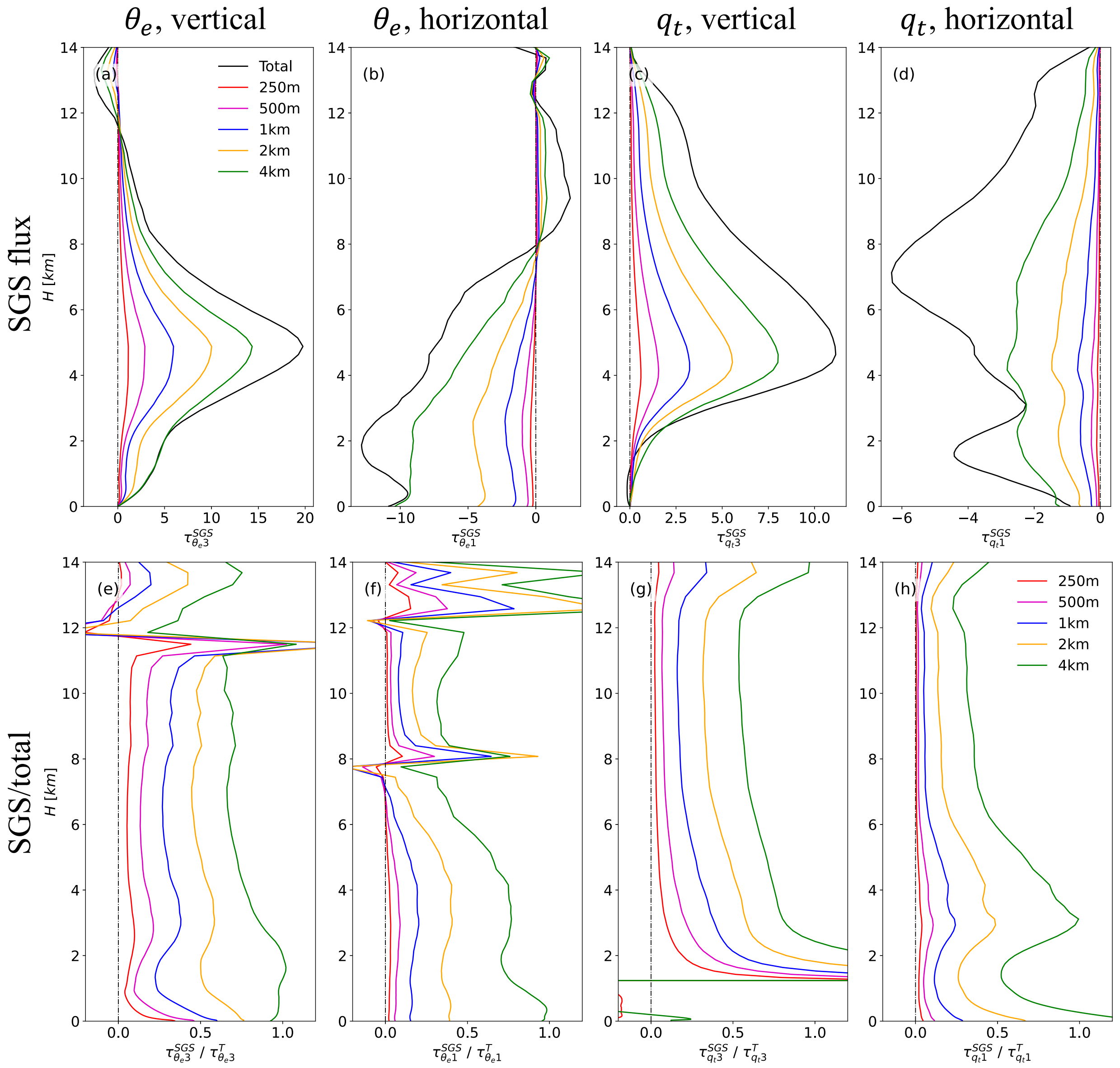

FIG. 3. Vertical profiles of the SGS fluxes of (a) $\tau_{\theta_e 3}^{\mathrm{SGS}}$ (K m s^{-1}), (b) $\tau_{\theta_e 1}^{\mathrm{SGS}}$ (K m s^{-1}), (c) $\tau_{q_t 3}^{\mathrm{SGS}}$ (g kg^{-1} m s^{-1}), and (d) $\tau_{q_t 1}^{\mathrm{SGS}}$ (g kg^{-1} m s^{-1}) by filtering the LES to different resolutions and (e)–(h) their ratios to the total turbulent fluxes $\tau_{\phi i}^{\mathrm{SGS}}/\tau_{\phi i}^{T}$. The total turbulent fluxes $\tau_{\phi i}^{T}$ are plotted in the top panels as reference. All profiles are spatially averaged between $x = -20$ km and $x = 5$ km and time averaged between hours 3 and 4.

use θ and q_v as the prognostic variables for SGS turbulent mixing. The comparison shows how nonconserved variables can exaggerate the occurrence of CG fluxes and advocates moist-conserved variables for SGS turbulence.

In the top row of Fig. 4, the overall distributions of the vertical DG and CG fluxes of θ_e are largely similar. Magnitude-wise, DG fluxes are larger between 4 and 6 km AGL (Fig. 4a), while CG fluxes are primarily responsible for the secondary maximum of $\tau_{\theta_e 3}^{\mathrm{SGS}}$ observed at the leading edge of the cold pool as shown in Fig. 2e. The percentage occurrence plot shown in Fig. 4c indicates that in the ascending region, almost half of the valid flux points show CG fluxes. The proportion further exceeds 60% in the leading edge of the cold pool indicating significant nonlocal transport.

The same analysis for $\tau_{\theta 3}^{\mathrm{SGS}}$ reveals a different picture as shown in the second row of Fig. 4. The vertical CG flux of θ (Fig. 4e) clearly dominates over the DG flux (Fig. 4d) with both larger values and broader spatial coverage. Comparing Fig. 4f with Fig. 4c, the percentage occurrence of CG fluxes is also greatly increased. Over 60% of the grid points are identified as CG fluxes within the squall-line updraft. The difference is due to inclusion of latent heating in the vertical θ_e fluxes. In other words, a substantial portion of the CG fluxes of θ shown

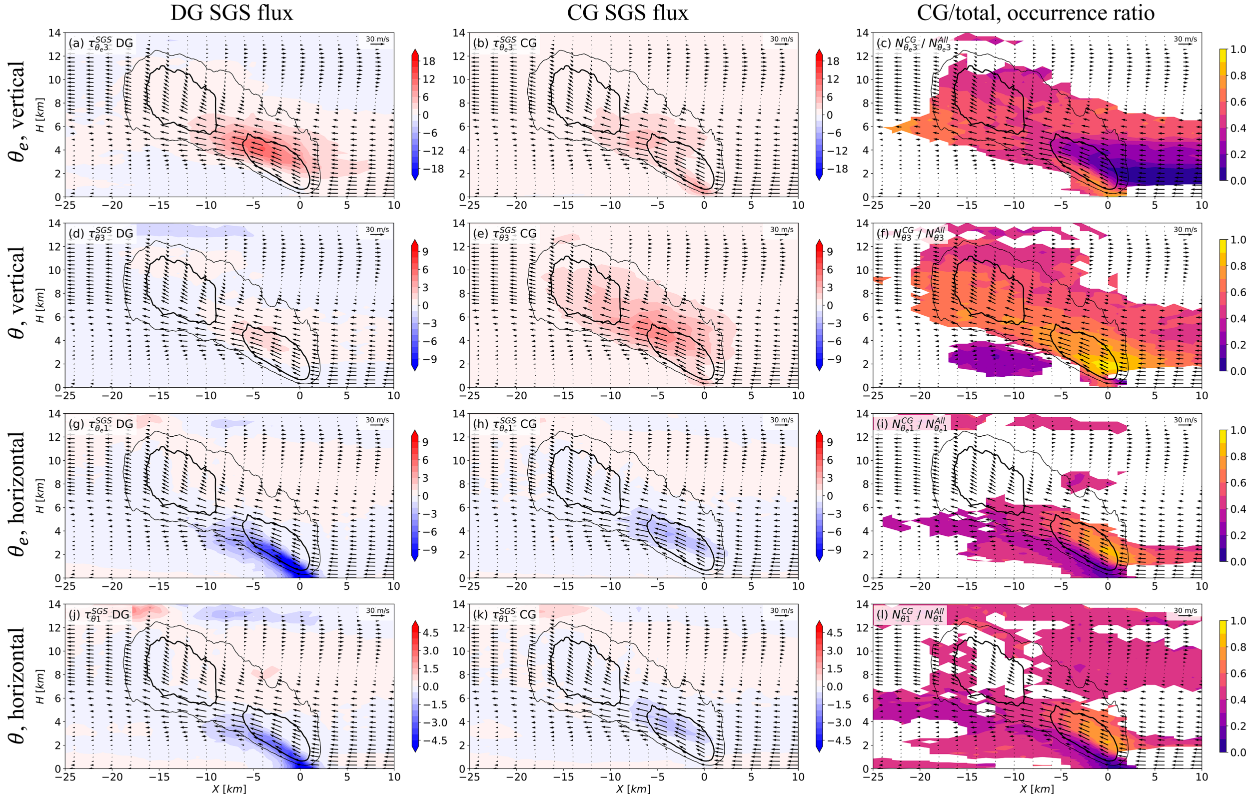

FIG. 4. Time- and along-line-averaged (left) downgradient and (middle) countergradient SGS fluxes of θ_e and θ in both the vertical and the horizontal directions. All fluxes are filtered to 1-km spacing, and the color scales are in units of kelvin meters per second. (right) The CG occurrence ratio $N^{\mathrm{CG}}/N^{\mathrm{ALL}}$, where regions with SGS fluxes of magnitude less than 0.5 K m s^{-1} are masked. DG and CG fluxes are defined by $\tau^{\mathrm{SGS}}_{\phi i}$ and $\partial\tilde{\phi}/\partial x_i$ having opposite and same signs, respectively.

in Fig. 4e is actually downgradient from θ_e's perspective, hence may still be parameterized by a gradient-diffusion closure based on θ_e. It is the CG θ_e fluxes shown in Fig. 4b that truly requires a non-gradient closure. It is also interesting to note that the DG fluxes of θ shown in Fig. 4d in the updraft core are upward positive, contrary to what one might image for a stably stratified environment. This is because at kilometer-scale resolutions, the CPMs are capable of (partially) resolving locally unstable regions ($\partial\tilde{\theta}/\partial z < 0$) in the updraft core, leading to upward DG fluxes.

As shown in Fig. 4g, the horizontal DG fluxes of θ_e are the most significant near the leading edge of the cold pool below 4 km AGL, while relatively large CG fluxes are found at 4-km height in the updraft core. The overall magnitude of the DG fluxes is larger than that of the CG fluxes. A budget analysis of $\tau^{\mathrm{SGS}}_{\theta_e 1}$ (not shown) reveals that the CG fluxes are produced by tilting production $\tau^{\mathrm{SGS}}_{\theta_e 3} \times \partial\tilde{u}/\partial z$, i.e., tilting of the vertical SGS flux $\tau^{\mathrm{SGS}}_{\theta_e 3}$ by the vertical wind shear into the horizontal direction. Note that in Strauss et al. (2019), horizontal CG heat fluxes were only found near the cloud top in a low-shear tropical setting. In this squall-line case, tilting of the updraft by the cold pool is responsible for the generation of horizontal CG fluxes. The occurrence ratio in Fig. 4i indicates that in the updraft below 4-km height, the proportion of grid points with CG horizontal fluxes generally exceeds 60% and even surpasses 80% in a small region at the inner core. The analysis performed on the horizontal θ flux in the bottom row of Fig. 4 reveals similar patterns, which is expected as horizontal movements of air parcels are not strongly tied to condensation as they are for vertical movements.

The same filtering and conditional sampling procedures are performed for the q_t fluxes. The vertical and the horizontal SGS fluxes of q_t are both significant as shown in the first column of Fig. 5, which together aligns with the tilted updraft. The distribution of SGS fluxes, their CG component, and the occurrence ratio in Fig. 5 reveal similar patterns as the θ_e fluxes shown in Figs. 2 and 4, except that the vertical SGS flux of θ_e remains countergradient at higher levels than that of q_t. The latter also tends to be more downgradient above 5 km AGL. The consistency between the CG occurrence ratios of θ_e and q_t fluxes (cf. Fig. 4c to Fig. 5c for the vertical ratio and Fig. 4i to Fig. 5f for the horizontal ratio) again highlights the importance of using conserved variables for the identification of CG fluxes. If one were to compare, say the CG occurrence ratios between q_t fluxes with θ fluxes, the different distribution patterns could mislead to dissimilarity arguments.

As shown in Figs. 4 and 5, the along-line-averaged SGS CG fluxes may point to the same directions as the DG fluxes. To gain a deeper understanding of this phenomenon, we show two vertical cross sections of the instantaneous flow fields at hour 4 of the simulation in Fig. 6. In the along-line cross

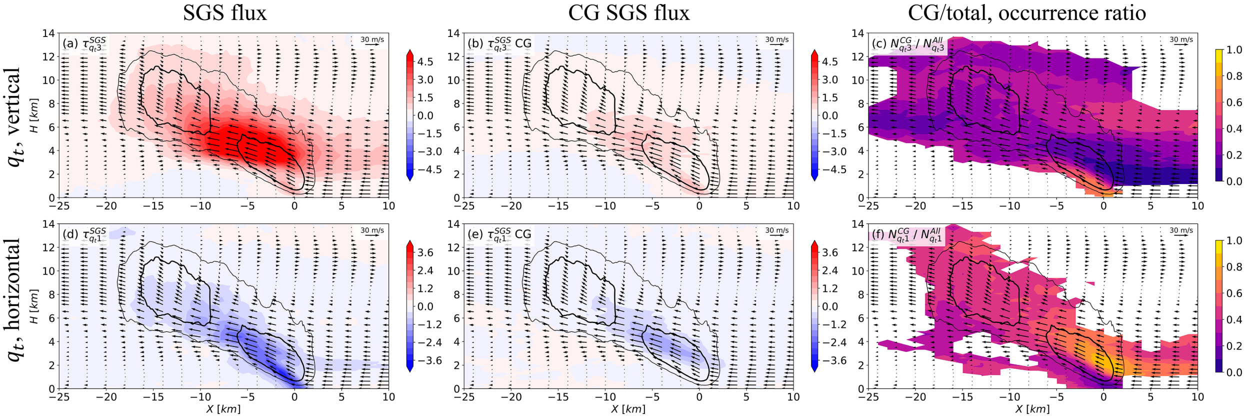

FIG. 5. As in Fig. 4, but for q_t fluxes (g kg^{-1} m s^{-1}). Regions with SGS fluxes of magnitude less than 0.2 g kg^{-1} m s^{-1} are masked in the CG occurrence ratio plots in the right column.

section (Fig. 6a), the average height of the inflow center ranges from 3 to 6 km AGL, characterized by high-θ_e values, with occasional strong updrafts reaching up to 8 km AGL. In this height range, the vertical SGS heat flux is predominantly positive, regardless of whether the location is above or below the center of high θ_e values. In other words, within the convective region, the vertical SGS heat transport is upward and shows no significant correlation with the local vertical gradient of θ_e, and the SGS flux can either be DG (above the local θ_e maxima) or CG (below the local θ_e maxima). In Fig. 6b, the inflow is associated with front-to-rear SGS heat flux (i.e., negative $\tau^{\mathrm{SGS}}_{\theta_e 1}$), with the high-$\theta_e$ values at the center of the inflow. Therefore, $\tau^{\mathrm{SGS}}_{\theta_e 1}$ at the rear side of the inflow center are DG, while the fluxes at the front side are CG. Considering the information presented in Fig. 2, a suitable interpretation is that squall line produces upward and front-to-rear turbulent heat fluxes overall. The structure of the squall-line system and the relative location within the system governs the direction of the SGS flux, with the local gradient of the scalar itself having a relatively minor impact.

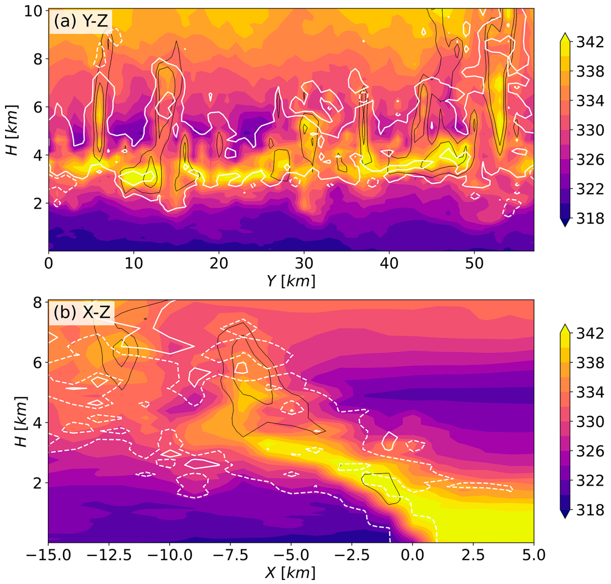

FIG. 6. Instantaneous vertical cross sections of θ_e (color shading), w (black lines for 10 and 15 m s^{-1} contours), and SGS θ_e fluxes (white dashed and solid lines denoting −5 and 5 K m s^{-1} contours, respectively), filtered to 1-km spacing at hour 4. (a) The $\tau^{\mathrm{SGS}}_{\theta_e 3}$ in the along-line direction at $x = -5$ km and (b) $\tau^{\mathrm{SGS}}_{\theta_e 1}$ in the cross-line direction at $y = 20$ km.

To further quantify the contribution of CG and DG fluxes at different heights, the 2D slices presented in Figs. 4 and 5 are averaged over the region between $x = -20$ km and $x = 5$ km to obtain vertical profiles of the θ_e and q_t fluxes along with their DG and CG components. The profiles presented in Fig. 7 offer a simplistic view of flux composition. For the vertical fluxes, countergradient SGS transport is comparable to downgradient transport for θ_e (Fig. 7a) at most heights but is less important for q_t (Fig. 7c). For the horizontal fluxes, DG fluxes dominate for both θ_e and q_t below 4 km and are comparable to CG fluxes above. Additionally, we note that the CG and DG fluxes are almost always aligned in the same direction, be it upward (positive) or downward (negative).

4. Evaluation of SGS closures

a. *Offline evaluation*

Based on the benchmark SGS fluxes presented in section 3, we conduct offline evaluation of the TKE and the Hgrad closures. The coarse-grained LES variables are inserted to the right-hand side of Eqs. (1)–(4) to obtain the diagnosed SGS fluxes from the two closures. The evaluation is conducted without performing actual simulations, so that the SGS closures do not affect the resolved flow (Pope 2000, chapter 13.4.6). Note that for the TKE closure, the SGS TKE is given by $e \equiv (1/2)\sum_{i=1}^{3}\widetilde{(u_i - \widetilde{u}_i)^2}$, and the coefficient C_K in Eq. (2) is multiplied by 3 so as to place the parameterized fluxes into the ballpark range of the benchmark fluxes. Compared to the LES benchmark in Fig. 2e, the TKE closure produces a rather small region of relatively weak upward fluxes (even after the tripling) centered at the updraft core below 6 km. Close examination of the horizontal distribution of $\tau^{\mathrm{TKE}}_{\theta_e 3}$ shows that

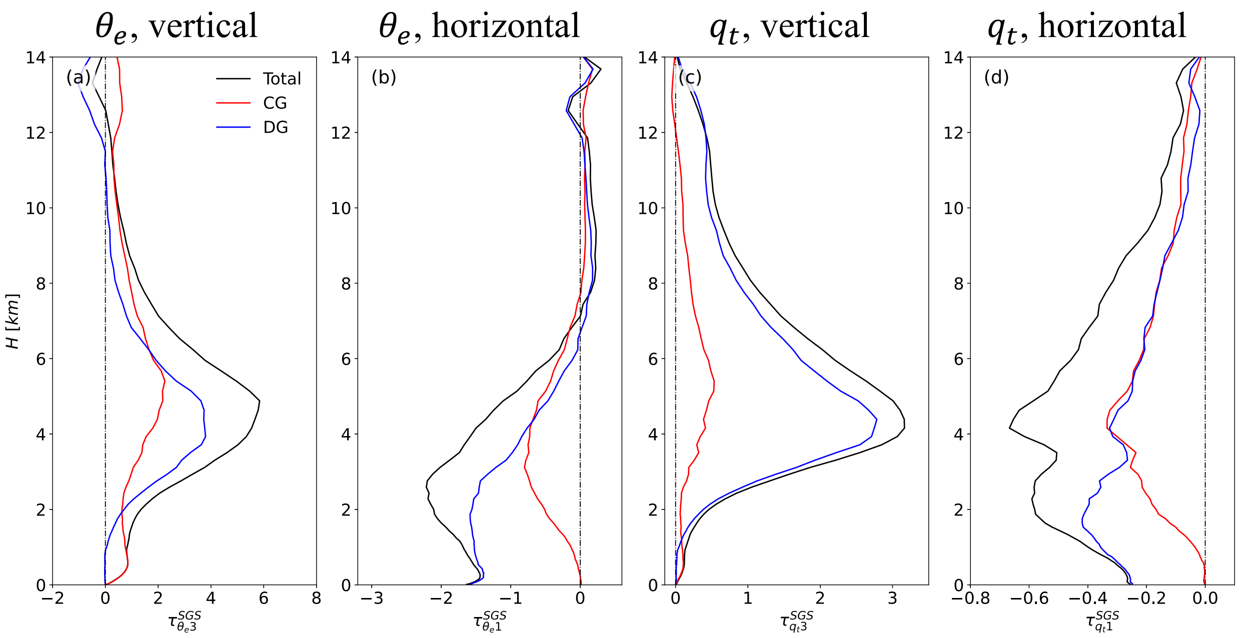

FIG. 7. Vertical profiles of (a) $\tau^{\mathrm{SGS}}_{\theta_e 3}$ (K m s^{-1}), (b) $\tau^{\mathrm{SGS}}_{\theta_e 1}$ (K m s^{-1}), (c) $\tau^{\mathrm{SGS}}_{q_t 3}$ (g kg^{-1} m s^{-1}), and (d) $\tau^{\mathrm{SGS}}_{q_t 1}$ (g kg^{-1} m s^{-1}) along with their CG and DG components at 1-km spacing. All profiles are spatially averaged between $x = -20$ km and $x = 5$ km and time averaged between hours 3 and 4.

the TKE closure misrepresents the positive CG fluxes for negative DG fluxes, which then offsets the true positive DG fluxes, leading to small line-averaged flux values. In comparison, the Hgrad closure in Fig. 8b well reproduces both the overall distribution and the magnitude of $\tau^{\mathrm{SGS}}_{\theta_e 3}$. For the horizontal fluxes, the performance of the TKE closure is in fact worse. Its inability to predict CG fluxes leads to a spurious rear-to-front SGS flux opposing the advective flux in upper half of the updraft region (cf. Fig. 8c to Fig. 4b). The Hgrad closure again reproduces the benchmark fluxes well (cf. Fig. 8d to Fig. 2f). Examination of the parameterized fluxes of q_t yields qualitatively similar results, hence are not shown for brevity.

The modeled fluxes in Fig. 8 are further averaged within -20 km $< x < 5$ km for quantitative evaluation. The resulting vertical profiles of the modeled fluxes of θ_e and q_t together with the filtered LES benchmark profiles from Fig. 7 are shown in Fig. 9. For $\tau^{\mathrm{SGS}}_{\theta_e 3}$ in Fig. 9a, the TKE closure predicts

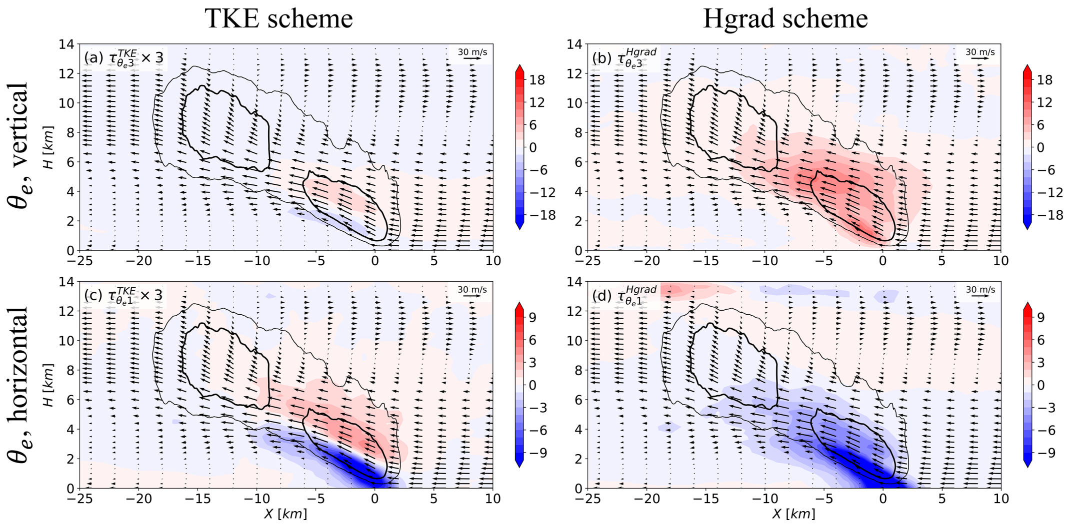

FIG. 8. Time- and along-line-averaged (top) $\tau^{\mathrm{SGS}}_{\theta_e 3}$ and (bottom) $\tau^{\mathrm{SGS}}_{\theta_e 1}$ modeled with the (left) TKE and the (right) Hgrad closures using coarse-grained LES to 1-km spacing. The color scales are in units of kelvin meters per second. Note that the TKE-modeled fluxes have been tripled to improve clarity.

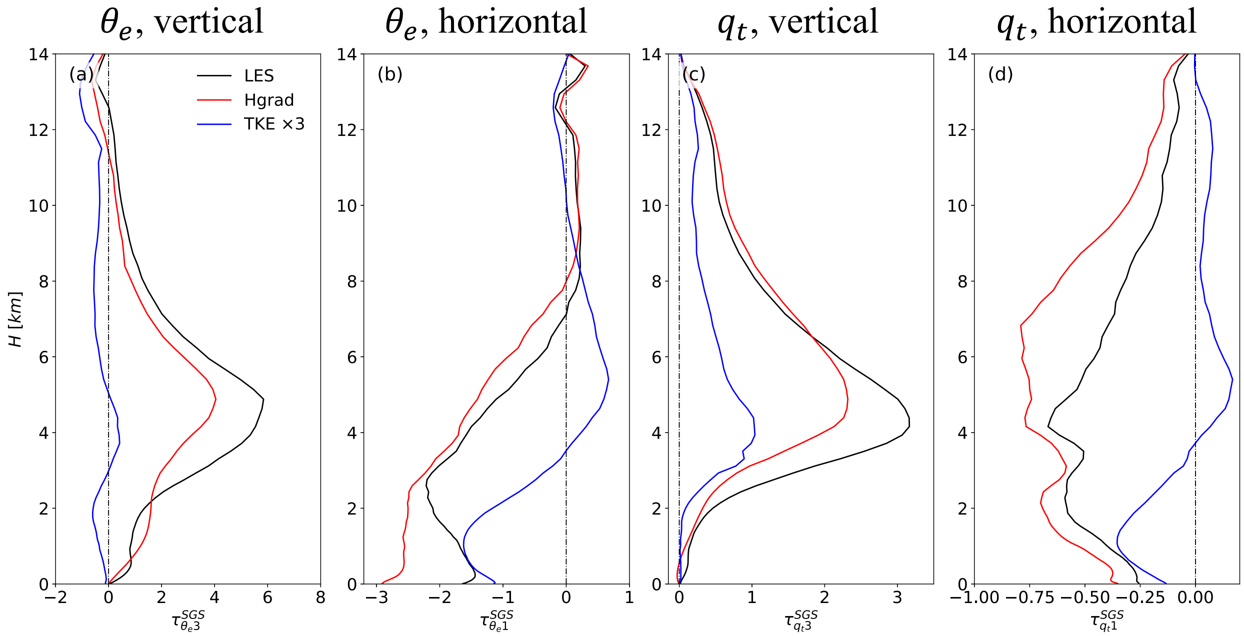

FIG. 9. As in Fig. 7, but for the diagnosed TKE and Hgrad fluxes from the coarse-grained LES to 1-km spacing.

vanishingly small values due to cancellation between the true DG flux and what should be CG but erroneously predicted as DG flux. For $\tau^{\mathrm{SGS}}_{\theta_e 1}$ in Fig. 9b, the TKE closure predicts a false positive flux between 4 and 8 km AGL, where the benchmark LES flux is negative. In comparison, the Hgrad closure performs fairly well, except for some mild underprediction of the peak $\tau^{\mathrm{SGS}}_{\theta_e 3}$ values and overprediction of $\tau^{\mathrm{SGS}}_{\theta_e 1}$ below 2-km height. The q_t-flux profiles in Figs. 9c and 9d largely corroborate the findings from the θ_e fluxes, again suggesting the improved performance of the Hgrad closure.

Next, we investigate whether the Hgrad closure is producing the right overall fluxes for the right reasons, i.e., whether τ^{Hgrad} has the right CG and DG composition. To do so, we decompose the Hgrad-modeled fluxes into DG and CG fluxes as we have done for the filtered LES fluxes and evaluate each component individually. The decomposed Hgrad fluxes are presented in Fig. 10; both the vertical and the horizontal fluxes show almost identical distributions to their respective benchmarks in Fig. 4. Even the occurrence rates of CG fluxes are well reproduced. The comparison rules out compensating errors, which often occur in SGS flux parameterizations where the overall effect of the parameterization scheme is correct, but each component does not agree with the actual physical term (see Zhou et al. 2018, for an example).

b. Online simulation

Next, we conduct online simulations of the squall line at kilometer-scale resolutions as described in section 2b. Compared to the offline evaluation, the online simulations allow full interactions between the SGS turbulence closure and the resolved flow and therefore provide a more objective assessment of the SGS closures (Pope 2000).

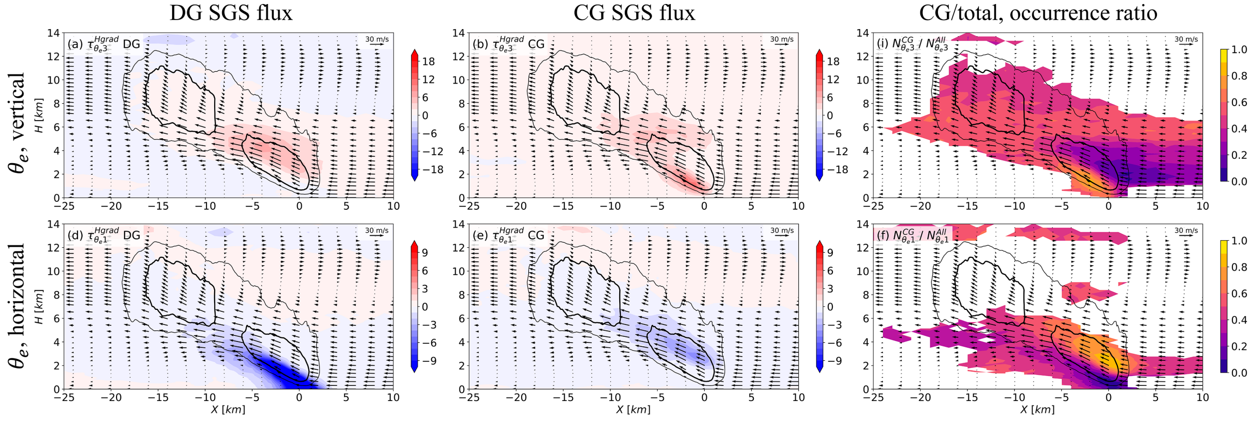

FIG. 10. As in Fig. 4, but for the diagnosed Hgrad fluxes from the coarse-grained LES to 1-km spacing.

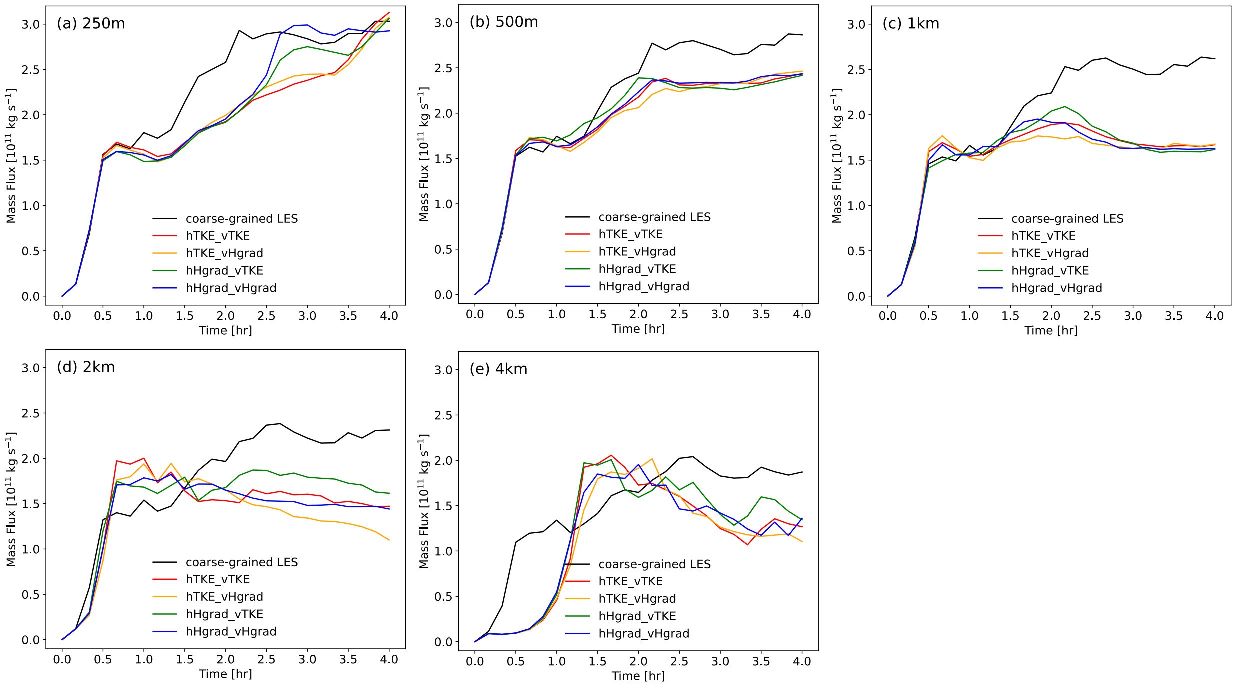

FIG. 11. Time series of updraft mass fluxes (kg s^{-1}) at different horizontal resolutions. The mass fluxes are calculated over the region where -80 km $< x < 40$ and 0 km $< y < 60$ km. Black lines denote the coarse-grained LES results.

The updraft mass flux (MF), defined as the domain total upward flux of dry air in Bryan and Morrison (2012), is calculated over the region where -80 km $< x < 40$ and 0 km $< y < 60$ km. The time series of MF for different resolutions are presented in Fig. 11. Note that the differences among the reference LES curves at different resolutions are caused by filtering. The evolution of the squall-line system in LES, as delineated by the changes in MF, can be divided into three distinct stages: an initial stage of convective triggering within 0.5 h, an intermediate stage characterized by development of the cold pool and the mesoscale circulation with increasing MF, and a final stage achieving quasi-equilibrium after approximately 2.0–2.5 h. This three-stage evolution is reproduced in simulations with 250-m (Fig. 11a) and 500-m (Fig. 11b) resolutions, although the latter produces smaller steady-state MF values.

As the resolution coarsens, the onset of initial convection is progressively delayed, and the MF values of the initial convection are increasingly overestimated. At 1-km resolution (Fig. 11c), the discrepancy between simulations and coarse-grained LES remains relatively minor. At 2 km (Fig. 11d), observable delays and significant overestimation (up to 40%) are found. At 4 km (Fig. 11e), the time required to trigger convection doubles compared to LES, with further intensification of updraft MF (up to 60%). This trend is consistent with the results in the convective boundary layers from Zhou et al. (2014), indicating resolution-dependent convective initiation at gray zone resolutions. The worsened MF predictions at 4-km resolutions have also been reported in Lai and Waite (2020) who evaluated gradient-diffusion closures in similar squall-line simulations. However, the delay in convective initiation was not significant in their study, potentially due to differences in the numerical setup.

Next, we observe the differences in the predicted MF by the different closures. In theory, if a vertical SGS scheme suppresses vertical transport, for example, the TKE scheme as shown in Fig. 9, the resolved flow should strengthen in compensation (Savazzi et al. 2025). Evidence of such compensation can be found at 2- and 4-km resolutions. Specifically, the two vTKE runs are associated with larger MF than their vHgrad counterparts especially at the mature stage (i.e., green line over blue line, red line over orange line). However, the differences are by no means significant nor are they clear at other resolutions. This reflects the challenges in the assessment of SGS closures at gray zone resolutions because flow is additionally constrained by the coarser resolution grid cells, posing difficulties to interpreting the accuracy of the resolved flow structure (Angevine et al. 2020). Overall, Fig. 11 shows that for grid sizes larger than 2 km, MF of the hHgrad_vTKE runs follows that of the coarse-grained LES more closely than those from other SGS closures, although differences are small and failed to pass the 0.05 significance level at 4-km resolution.

To assess the overall objective skill of the turbulence closures, Fig. 12 presents the root-mean-square errors (RMSEs) of six key dynamical and thermodynamical variables, evaluated against the filtered LES data. The RMSEs for all variables increase with coarser resolution except for the vertical velocity w. This is because the absolute value of w decreases to zero as the grid spacing coarsens. In general, different schemes exhibit varying RMSEs for each variable at different resolutions, although the differences are oftentimes insignificant. But more

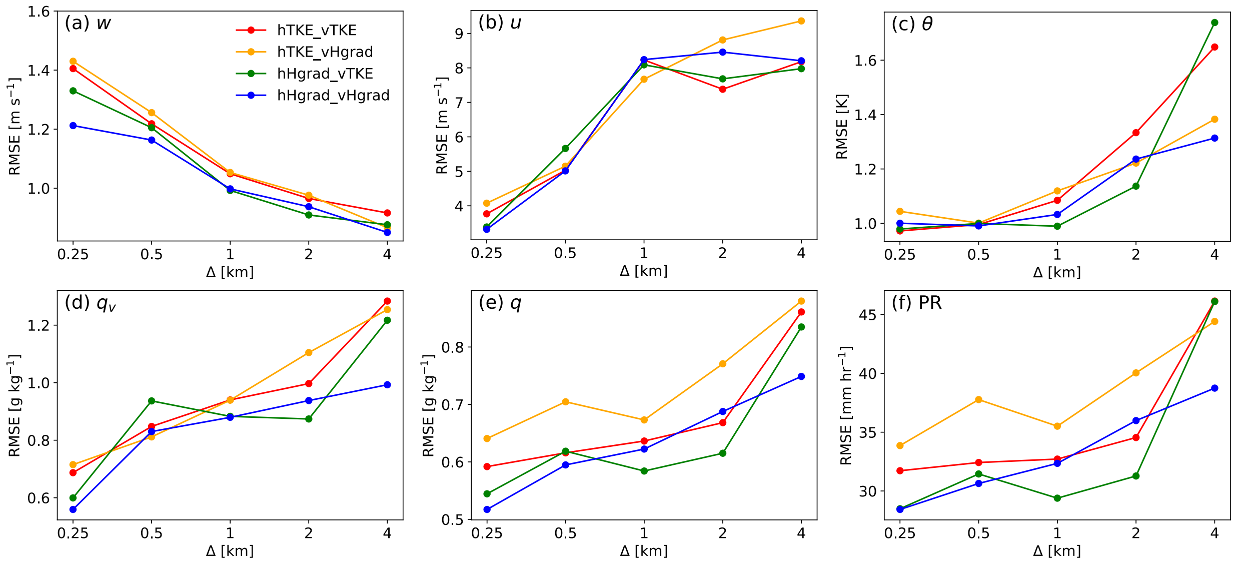

FIG. 12. Variations of the RMSEs for the (a) vertical velocity w (m s^{-1}), (b) streamwise wind u (m s^{-1}), (c) potential temperature θ (K), (d) water vapor mixing ratio q_v (g kg^{-1}), (e) hydrometeor contents q (g kg^{-1}), and (f) precipitation rate PR (mm h^{-1}) with grid spacing. The RMSEs are computed based on the filtered LES data at hour 4 and in the region between -40 km $< x <$ 40 km. For (a)–(e), volume-averaged statistics under 8 km AGL are used.

often than not, the hHgrad simulations (blue and green lines) show lower RMSEs than the hTKE simulations (red and orange lines). For example, at 4-km resolutions, the RMSE of the hHgrad model (blue line) is the smallest for θ, q_v, q, and precipitation rate (PR) in Figs. 12c–f.

Compared to the default TKE closure (hTKE_vTKE; red lines in Fig. 12), adopting the Hgrad closure in the vertical direction only (hTKE_vHgrad; orange lines) does not appear to be a good choice, as the latter leads to equally large and sometimes larger RMSEs. On the contrary, when the Hgrad closure is only applied to the horizontal fluxes in the hHgrad_vTKE closure (green lines), improvements are observed for the flow (Fig. 12b), the thermodynamic (Fig. 12c), and the moisture fields (Figs. 12d,e), as well as for surface precipitation (Fig. 12f) at 1- and 2-km resolutions. While at 4-km resolutions, the improvements are rather limited and sometimes even reversed (Figs. 12c,f). The 3D Hgrad closure (hHgrad_vHgrad; blue lines) leads to modest improvements at 1- and 2-km horizontal resolutions compared to the hHgrad_vTKE closure, but their performance at 4-km resolution is consistently the best among the four closures.

To further evaluate SGS turbulence closures in the simulating storm structure, we examine the emulated radar reflectivity and the cold pool. Along-line-averaged radar reflectivity and the θ' fields from the LES at the end of hour 4 are presented in Fig. 13 to serve as benchmark references. Given the idealized setup (section 2b), the reflectivity field and the cold pool in Fig. 13 exhibit classic textbook structures of squall lines (see, e.g., Markowski and Richardson 2010). Figures 14 and 15 present the simulated reflectivity and the cold pool, respectively, using the four closures at 250-m and 1-km grid spacings.

At 250-m grid spacing, all runs are capable of reproducing the overall reflectivity and cold pool structures as those simulated by the LES, although the details differ. In Figs. 14e and 14g, when the Hgrad closure is applied to the horizontal fluxes, the updrafts are stronger and the reflectivity values within the convective core are larger compared to those from the TKE closure (Fig. 14a). In comparison, the hTKE_vHgrad closure

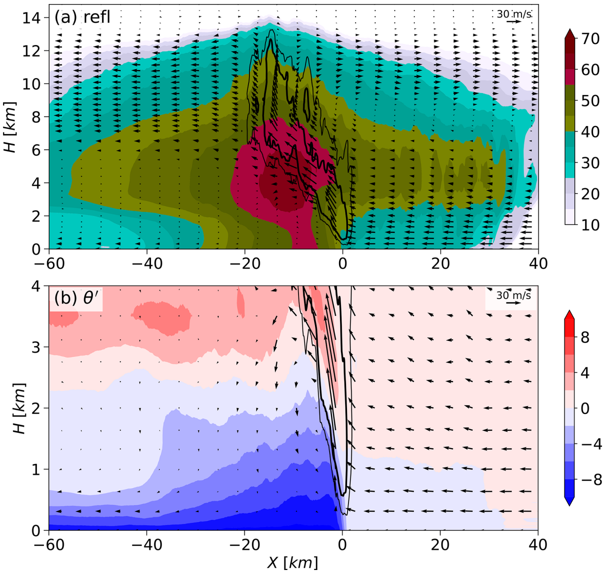

FIG. 13. Along-line-averaged (a) radar reflectivity (dBZ) and (b) potential temperature perturbation θ' (K) from the inflow in the LES. The snapshot is taken at hour 4 of the simulation. The lines and arrows take on the same meaning as in Fig. 1.

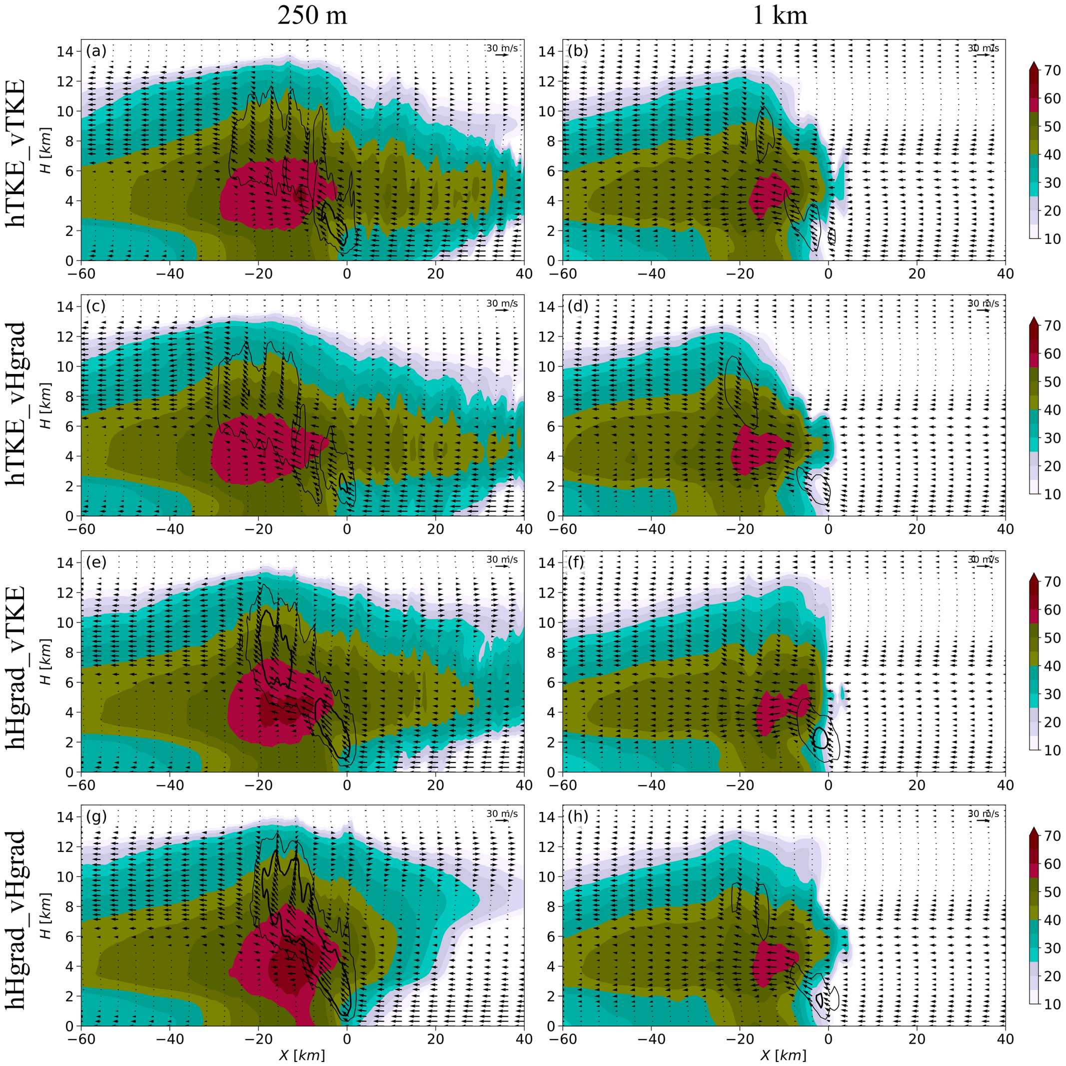

FIG. 14. As in Fig. 13a, but for (left) Δ = 250-m and (right) Δ = 1-km simulations using different SGS closures.

produces a rather weak updraft, and the greater-than-60-dBZ region (magenta shading) vanishes almost completely. Similarly, simulations with the TKE closure for the horizontal fluxes (Figs. 15a,c) produce weaker cold pools compared to those adopting the Hgrad closure (Figs. 15e,g). The relatively weak potential temperature gradient across the cold pool head in the two hTKE runs suggest reduced surface confluence in accordance with weaker updrafts.

At 1-km resolution (right column of Fig. 14), the simulated reflectivity structure as well as the updraft strength show larger differences from the LES. Such deterioration fits the description of the "dark gray zone" proposed by Angevine et al. (2020), where closures become most indefensible. A similar result was presented in Bryan et al. (2003, their Fig. 6), where the rainwater mixing ratio (similar to reflectivity) underwent drastic changes from 500-m to 1-km resolution. Among the four closures, the hHgrad closures are slightly better than the hTKE closures, where the most intense dBZ regions are slightly larger, and the updrafts are slightly stronger. The cold pool structures in the right column of Fig. 15 also suggest that the horizontal closures make some difference. The two hTKE runs simulate rearward sloping cold pools with a 9.1° slope angle between $x = -3$ km and $x = 0$ for hTKE_vTKE and 17.4° for hTKE_vHgrad, whereas the hHgrad runs produce steep cold pools (~20°) that are able to support more erect updrafts and are closer to the LES tilt (~27°). The results at 4-km resolution are qualitatively similar to those at 1 km, hence not shown. While the hHgrad runs are slightly better than the hTKE runs, the improvements are clearly not enough to make up for the further weakening of the storms as governed by the resolution.

5. Summary and conceptual schematic

Based on the coarse graining of an idealized large-eddy simulation of a squall line, we investigate the characteristics of subgrid-scale fluxes on kilometer-scale grids. First and foremost, it is found that SGS heat and moisture fluxes dominate

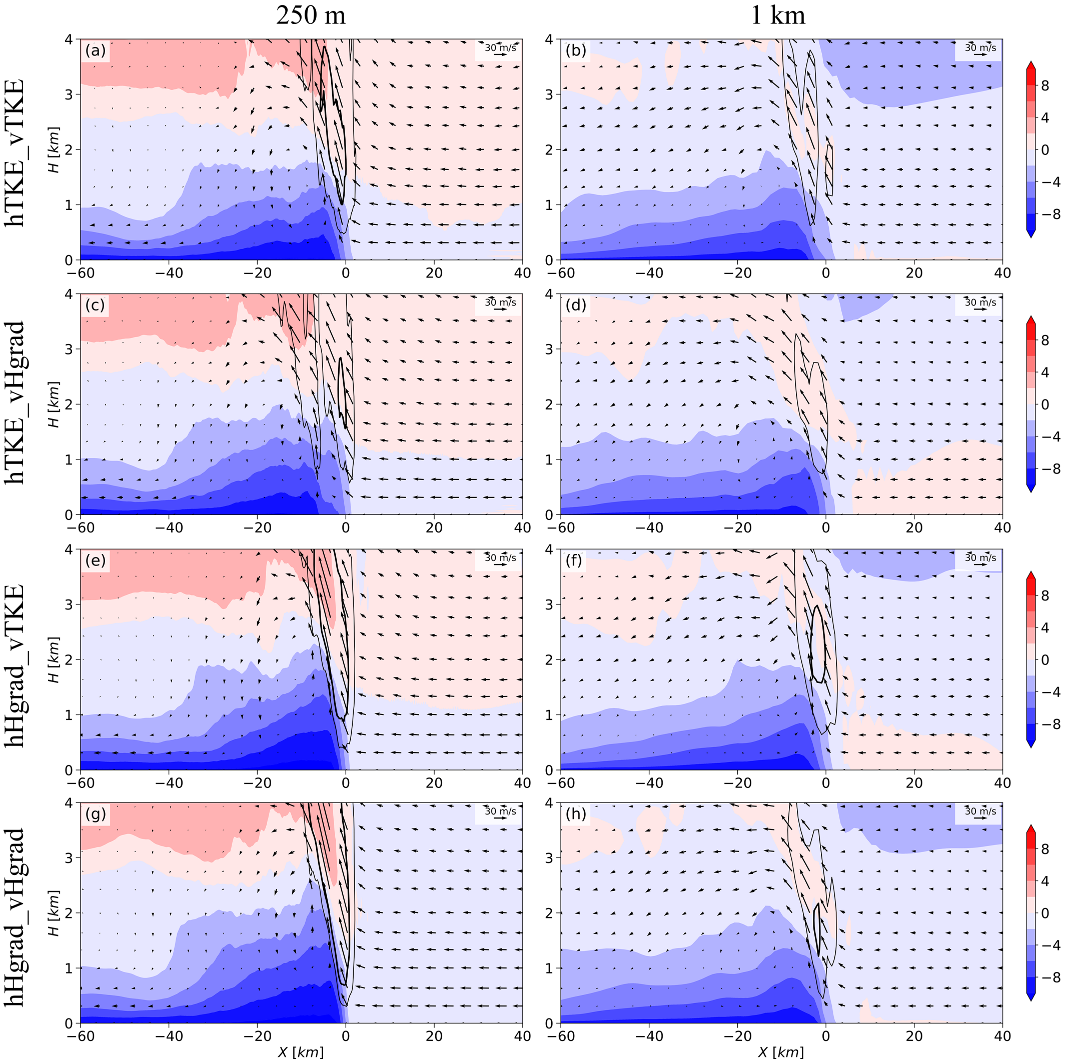

FIG. 15. As in Fig. 13b, but for (left) Δ = 250-m and (right) Δ = 1-km simulations using different SGS closures.

over the resolved fluxes at 4-km spacings. With increased resolution, their contributions decrease systematically (~50% at 2-km spacing and ~20% at 1-km spacing). At 500-m and finer spacings, the resolved fluxes are mostly responsible for the turbulent transport. For the SGS fluxes, we found significant countergradient vertical SGS fluxes in the updraft region, indicative of nonlocal transport by organized convection as reported in previous studies. However, using moist-conserved variables (θ_e and q_t) to avoid ambiguity associated with latent heating and phase changes, our estimate of the proportion of CG fluxes are significantly less than estimates based on nonconserved variables such as θ and q_v. At 1-km resolution, DG and CG fluxes contribute comparably to the total SGS flux in the updraft region of the simulated squall line. Moreover, DG and CG vertical fluxes show similar spatial distribution and both point to the same upward direction.

In addition to vertical SGS fluxes, we found that horizontal SGS fluxes in kilometer-scale squall-line simulations are also characterized by the significant CG transport. It is the nonlocal transport by the tilted updrafts that are responsible for the CG transport in both the vertical and the horizontal directions. Unlike the vertical fluxes, DG and CG *horizontal* transport are spatially separated. The former is dominant on the leading edge of the cold pool, while the latter sits on top of the former and largely overlap with the updraft. Again, both fluxes point to the rearward direction, indicating efficient turbulent transport compared to a scenario where the two fluxes counteract each other by pointing in opposite directions.

Contrary to the central role of vertical SGS fluxes in former studies of kilometer-scale simulations of upright tropical convection, the offline analyses in section 4a highlight the effect of horizontal SGS fluxes for convection-permitting simulations of tilted storms, suggesting the importance of accurate representation of horizontal fluxes, especially their CG components. The online simulations in section 4b show improvements in bulk RMSE statistics with the Hgrad closure than with the TKE closure as predicted by the offline analyses,

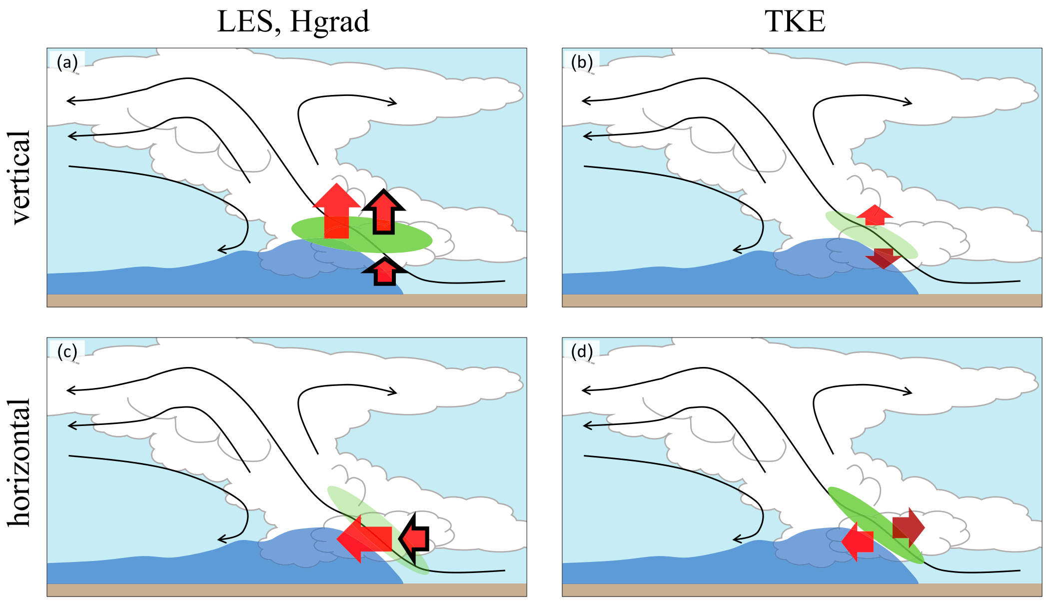

FIG. 16. Conceptual schematics depicting the impact of (a),(b) vertical and (c),(d) horizontal SGS fluxes to kilometer-scale squall-line simulations. Red arrows with and without outlines denote CG and DG fluxes, respectively. Brown arrows in (b) and (d) denote the erroneously predicted DG fluxes by the TKE closure. Green ellipses indicate regions of divergent SGS fluxes, with darker color for larger divergence. Blue shading represents the surface cold pool.

although the advantages of using the Hgrad closure for the horizontal flux do not appear critical.

A conceptual schematic on the influences of turbulence closures for the 3D fluxes in a kilometer-scale squall-line simulation is depicted in Fig. 16 to help tie the analyses together. In the vertical direction as shown in Fig. 16a, a flux divergence zone (indicated by green shading) is found over the updraft region that together with vertical advection balances latent heating. The vertical fluxes are contributed comparably by the DG and the CG fluxes at higher levels, while the latter dominates below 2 km (see Figs. 4a,b). The TKE closure, as limited by its gradient-diffusion construct, produces an underestimated upward flux and a spurious downward flux. The small upward flux is a result of the erroneously parameterized CG flux as DG flux. Despite the opposing fluxes above and below the updraft, the resulting flux divergence is actually weaker with the TKE closure, as the magnitudes of the fluxes predicted by the TKE closure are rather small (see Fig. 8a).

As shown in Fig. 16c, the horizontal flux is directed rearward along the tilted updraft. A slanted zone of horizontal flux divergence is also present at the updraft location. The divergent fluxes reduce convective energy and serve to balance the latent heating. The rear and front sides of the flux divergence zone are dominated by DG and CG fluxes, respectively, as shown in Figs. 4g and 4h. While the TKE closure is able to simulate DG fluxes along the cold pool edge, its inability to simulate CG fluxes leads to a spurious rear-to-front flux ahead of the updraft (Fig. 16d). As a result, horizontal flux divergence is greatly enhanced, leading to excessive cooling and drying of the updraft. This explains the weaker storms (Figs. 14 and 15) when the horizontal fluxes are parameterized by the TKE closure.

Based on the schematic, we can also understand why improving the vertical fluxes alone (i.e., the vHgrad_hTKE runs) deteriorates the simulations and leads to the weakest storm as shown in Figs. 12, 14, and 15. This is because this particular combination leads to the strongest flux divergence, hence the excessive cooling and drying of the updraft. The TKE run (i.e., vTKE_hTKE) is slightly better than the vHgrad_hTKE run because the reduced vertical flux divergence (associated with the wrong representation of vertical fluxes) ameliorates the excessive horizontal flux divergence, which makes it an improvement by compensating errors. Therefore, for kilometer-scale simulations of convective storms, especially with grid spacing greater than 1 km, it is useful to improve the parameterization of both the vertical and the horizontal SGS fluxes. Improving the vertical SGS parameterization alone does not necessarily guarantee model improvements, especially when the main convective updrafts are tilted. In these cases, horizontal fluxes may play a bigger role and may require more accurate representation by an SGS closure that accommodates countergradient transport.

Acknowledgments. We thank Dr. Xiaochen Zhang and Professor Xin Xu for helpful discussions. We are also grateful to the three anonymous peer reviewers for their constructive suggestions. This work is supported by the National Natural Science Foundation of China (Grant 42105151), the Jiangsu Provincial Science and Technology Support Plan Social Development General Project (Grant BE2022851), and the Basic Research Fund of the China Academy of Meteorological Sciences (Grant 2021Y008). Numerical simulations were carried out at National Supercomputing Center in Tianjin. Some analyses were also supported by the National Large Scientific and Technological Infrastructure "Earth System Numerical Simulation Facility" (https://cstr.cn/31134.02.EL).

Data availability statement. The source codes of the modified ARPS model and the input setting files for the simulations used in this work are publicly available at Zenodo at https://doi.org/10.5281/zenodo.11188707. The Python scripts to filter the LES were also included.

REFERENCES

Angevine, W. M., J. Olson, J. J. Gristey, I. Glenn, G. Feingold, and D. D. Turner, 2020: Scale awareness, resolved circulations, and practical limits in the MYNN–EDMF boundary layer and shallow cumulus scheme. *Mon. Wea. Rev.*, **148**, 4629–4639, https://doi.org/10.1175/MWR-D-20-0066.1.

Arakawa, A., and C.-M. Wu, 2013: A unified representation of deep moist convection in numerical modeling of the atmosphere. Part I. *J. Atmos. Sci.*, **70**, 1977–1992, https://doi.org/10.1175/JAS-D-12-0330.1.

Benjamin, S. G., J. M. Brown, G. Brunet, P. Lynch, K. Saito, and T. W. Schlatter, 2018: 100 years of progress in forecasting and NWP applications. A Century of Progress in Atmospheric and Related Sciences: Celebrating the American Meteorological Society Centennial, Meteor. Monogr., No. 59, Amer. Meteor. Soc., https://doi.org/10.1175/AMSMONOGRAPHS-D-18-0020.1.

Bryan, G. H., 2005: Spurious convective organization in simulated squall lines owing to moist absolutely unstable layers. *Mon. Wea. Rev.*, **133**, 1978–1997, https://doi.org/10.1175/MWR2952.1.

——, and H. Morrison, 2012: Sensitivity of a simulated squall line to horizontal resolution and parameterization of microphysics. *Mon. Wea. Rev.*, **140**, 202–225, https://doi.org/10.1175/MWR-D-11-00046.1.

——, J. C. Wyngaard, and J. M. Fritsch, 2003: Resolution requirements for the simulation of deep moist convection. *Mon. Wea. Rev.*, **131**, 2394–2416, https://doi.org/10.1175/1520-0493(2003)131<2394:RRFTSO>2.0.CO;2.

Clark, P., N. Roberts, H. Lean, S. P. Ballard, and C. Charlton-Perez, 2016: Convection-permitting models: A step-change in rainfall forecasting. *Meteor. Appl.*, **23**, 165–181, https://doi.org/10.1002/met.1538.

Clark, R. A., J. H. Ferziger, and W. C. Reynolds, 1977: Evaluation of subgrid-scale turbulence models using a fully simulated turbulent flow. NASA STI/Recon Tech. Rep. TF-9, 127 pp., https://ntrs.nasa.gov/api/citations/19770014415/downloads/19770014415.pdf.

——, ——, and ——, 1979: Evaluation of subgrid-scale models using an accurately simulated turbulent flow. *J. Fluid Mech.*, **91**, 1–16, https://doi.org/10.1017/S002211207900001X.

Deardorff, J. W., 1966: The counter-gradient heat flux in the lower atmosphere and in the laboratory. *J. Atmos. Sci.*, **23**, 503–506, https://doi.org/10.1175/1520-0469(1966)023<0503:TCGHFI>2.0.CO;2.

——, 1980: Stratocumulus-capped mixed layers derived from a three-dimensional model. *Bound.-Layer Meteor.*, **18**, 495–527, https://doi.org/10.1007/BF00119502.

Emanuel, K. A., 1994: *Atmospheric Convection.* Oxford University Press, 580 pp., https://doi.org/10.1093/oso/9780195066302.001.0001.

Fan, J., and Coauthors, 2017: Cloud-resolving model intercomparison of an MC3E squall line case: Part I—Convective updrafts. *J. Geophys. Res. Atmos.*, **122**, 9351–9378, https://doi.org/10.1002/2017JD026622.

Fiori, E., A. Parodi, and F. Siccardi, 2010: Turbulence closure parameterization and grid spacing effects in simulated supercell storms. *J. Atmos. Sci.*, **67**, 3870–3890, https://doi.org/10.1175/2010JAS3359.1.

Green, B. W., and F. Zhang, 2015: Numerical simulations of Hurricane Katrina (2005) in the turbulent gray zone. *J. Adv. Model. Earth Syst.*, **7**, 142–161, https://doi.org/10.1002/2014MS000399.

Hanley, K., M. Whitall, A. Stirling, and P. Clark, 2019: Modifications to the representation of subgrid mixing in kilometre-scale versions of the unified model. *Quart. J. Roy. Meteor. Soc.*, **145**, 3361–3375, https://doi.org/10.1002/qj.3624.

Holtslag, A. A. M., and C.-H. Moeng, 1991: Eddy diffusivity and countergradient transport in the convective atmospheric boundary layer. *J. Atmos. Sci.*, **48**, 1690–1698, https://doi.org/10.1175/1520-0469(1991)048<1690:EDACTI>2.0.CO;2.

Honnert, R., V. Masson, and F. Couvreux, 2011: A diagnostic for evaluating the representation of turbulence in atmospheric models at the kilometric scale. *J. Atmos. Sci.*, **68**, 3112–3131, https://doi.org/10.1175/JAS-D-11-061.1.

Houze, R. A., 1993: *Cloud Dynamics.* Academic Press, 573 pp.

Jensen, A. A., J. Y. Harrington, and H. Morrison, 2018: Microphysical characteristics of squall-line stratiform precipitation and transition zones simulated using an ice particle property-evolving model. *Mon. Wea. Rev.*, **146**, 723–743, https://doi.org/10.1175/MWR-D-17-0215.1.

Kain, J. S., 2004: The Kain–Fritsch convective parameterization: An update. *J. Appl. Meteor.*, **43**, 170–181, https://doi.org/10.1175/1520-0450(2004)043<0170:TKCPAU>2.0.CO;2.

Kendon, E. J., A. F. Prein, C. A. Senior, and A. Stirling, 2021: Challenges and outlook for convection-permitting climate modelling. *Philos. Trans. Roy. Soc.*, **A379**, 20190547, https://doi.org/10.1098/rsta.2019.0547.

Lafore, J.-P., and M. W. Moncrieff, 1989: A numerical investigation of the organization and interaction of the convective and stratiform regions of tropical squall lines. *J. Atmos. Sci.*, **46**, 521–544, https://doi.org/10.1175/1520-0469(1989)046<0521:ANIOTO>2.0.CO;2.

Lai, K. T., and M. L. Waite, 2020: Resolution dependence and subfilter-scale motions in idealized squall-line simulations. *Mon. Wea. Rev.*, **148**, 3059–3078, https://doi.org/10.1175/MWR-D-19-0330.1.

Langhans, W., J. Schmidli, and C. Schär, 2012: Mesoscale impacts of explicit numerical diffusion in a convection-permitting model. *Mon. Wea. Rev.*, **140**, 226–244, https://doi.org/10.1175/2011MWR3650.1.

Lean, H. W., P. A. Clark, M. Dixon, N. M. Roberts, A. Fitch, R. Forbes, and C. Halliwell, 2008: Characteristics of high-resolution versions of the Met Office Unified Model for forecasting convection over the United Kingdom. *Mon. Wea. Rev.*, **136**, 3408–3424, https://doi.org/10.1175/2008MWR2332.1.

Lebo, Z. J., and H. Morrison, 2015: Effects of horizontal and vertical grid spacing on mixing in simulated squall lines and implications for convective strength and structure. *Mon. Wea. Rev.*, **143**, 4355–4375, https://doi.org/10.1175/MWR-D-15-0154.1.

Lin, Y.-L., R. D. Farley, and H. D. Orville, 1983: Bulk parameterization of the snow field in a cloud model. *J. Climate Appl. Meteor.*, **22**, 1065–1092, https://doi.org/10.1175/1520-0450(1983)022<1065:BPOTSF>2.0.CO;2.

Liu, C., M. W. Moncrieff, and W. W. Grabowski, 2001: Explicit and parameterized realizations of convective cloud systems in TOGA COARE. *Mon. Wea. Rev.*, **129**, 1689–1703, https://doi.org/10.1175/1520-0493(2001)129<1689:EAPROC>2.0.CO;2.

Liu, M., and B. Zhou, 2022: Variations of subgrid-scale turbulent fluxes in the dry convective boundary layer at gray zone resolutions. *J. Atmos. Sci.*, **79**, 3245–3261, https://doi.org/10.1175/JAS-D-22-0085.1.

Markowski, P., and Y. Richardson, 2010: *Mesoscale Meteorology in Midlatitudes.* 1st ed. Wiley, 407 pp., https://onlinelibrary.wiley.com/doi/book/10.1002/9780470682104.

Moeng, C.-H., 1984: A large-eddy-simulation model for the study of planetary boundary-layer turbulence. *J. Atmos. Sci.*, **41**, 2052–2062, https://doi.org/10.1175/1520-0469(1984)041<2052:ALESMF>2.0.CO;2.

——, 2014: A closure for updraft–downdraft representation of subgrid-scale fluxes in cloud-resolving models. *Mon. Wea. Rev.*, **142**, 703–715, https://doi.org/10.1175/MWR-D-13-00166.1.

——, P. P. Sullivan, M. F. Khairoutdinov, and D. A. Randall, 2010: A mixed scheme for subgrid-scale fluxes in cloud-resolving models. *J. Atmos. Sci.*, **67**, 3692–3705, https://doi.org/10.1175/2010JAS3565.1.

Morrison, H., G. Thompson, and V. Tatarskii, 2009: Impact of cloud microphysics on the development of trailing stratiform precipitation in a simulated squall line: Comparison of one- and two-moment schemes. *Mon. Wea. Rev.*, **137**, 991–1007, https://doi.org/10.1175/2008MWR2556.1.

Pearson, K. J., R. J. Hogan, R. P. Allan, G. M. S. Lister, and C. E. Holloway, 2010: Evaluation of the model representation of the evolution of convective systems using satellite observations of outgoing longwave radiation. *J. Geophys. Res.*, **115**, D20206, https://doi.org/10.1029/2010JD014265.

Pope, S. B., 2000: *Turbulent Flows.* Cambridge University Press, 771 pp.

Prein, A. F., and Coauthors, 2015: A review on regional convection-permitting climate modeling: Demonstrations, prospects, and challenges. *Rev. Geophys.*, **53**, 323–361, https://doi.org/10.1002/2014RG000475.

Rotunno, R., J. B. Klemp, and M. L. Weisman, 1988: A theory for strong, long-lived squall lines. *J. Atmos. Sci.*, **45**, 463–485, https://doi.org/10.1175/1520-0469(1988)045<0463:ATFSLL>2.0.CO;2.

Savazzi, A. C. M., L. Nuijens, W. de Rooy, and A. P. Siebesma, 2025: The influence of parameterized shallow convection on trade-wind clouds and circulations in the HARMONIE-AROME mesoscale model. *J. Adv. Model. Earth Syst.*, **17**, e2024MS004538, https://doi.org/10.1029/2024MS004538.

Schwartz, C. S., and Coauthors, 2009: Next-day convection-allowing WRF model guidance: A second look at 2-km versus 4-km grid spacing. *Mon. Wea. Rev.*, **137**, 3351–3372, https://doi.org/10.1175/2009MWR2924.1.

Shi, X., and Y. Wang, 2022: Impacts of cumulus convection and turbulence parameterizations on the convection-permitting simulation of typhoon precipitation. *Mon. Wea. Rev.*, **150**, 2977–2997, https://doi.org/10.1175/MWR-D-22-0057.1.

——, F. K. Chow, R. L. Street, and G. H. Bryan, 2019: Key elements of turbulence closures for simulating deep convection at kilometer-scale resolution. *J. Adv. Model. Earth Syst.*, **11**, 818–838, https://doi.org/10.1029/2018MS001446.

Siebesma, A. P., P. M. M. Soares, and J. Teixeira, 2007: A combined eddy-diffusivity mass-flux approach for the convective boundary layer. *J. Atmos. Sci.*, **64**, 1230–1248, https://doi.org/10.1175/JAS3888.1.

Skamarock, W. C., J. B. Klemp, M. G. Duda, L. D. Fowler, S.-H. Park, and T. D. Ringler, 2012: A multiscale nonhydrostatic atmospheric model using centroidal Voronoi tesselations and C-grid staggering. *Mon. Wea. Rev.*, **140**, 3090–3105, https://doi.org/10.1175/MWR-D-11-00215.1.

——, and Coauthors, 2021: A description of the Advanced Research WRF Model version 4.3. NCAR Tech. Note NCAR/TN-556+STR, 165 pp., https://doi.org/10.5065/1dfh-6p97.

Smagorinsky, J., 1963: General circulation experiments with the primitive equations. *Mon. Wea. Rev.*, **91**, 99–164, https://doi.org/10.1175/1520-0493(1963)091<0099:GCEWTP>2.3.CO;2.

Strauss, C., D. Ricard, C. Lac, and A. Verrelle, 2019: Evaluation of turbulence parametrizations in convective clouds and their environment based on a large-eddy simulation. *Quart. J. Roy. Meteor. Soc.*, **145**, 3195–3217, https://doi.org/10.1002/qj.3614.

Sullivan, P. P., and E. G. Patton, 2011: The effect of mesh resolution on convective boundary layer statistics and structures generated by large-eddy simulation. *J. Atmos. Sci.*, **68**, 2395–2415, https://doi.org/10.1175/JAS-D-10-05010.1.

Sun, S., B. Zhou, M. Xue, and K. Zhu, 2021: Scale-similarity subgrid-scale turbulence closure for supercell simulations at kilometer-scale resolutions: Comparison against a large-eddy simulation. *J. Atmos. Sci.*, **78**, 417–437, https://doi.org/10.1175/JAS-D-20-0187.1.

Takemi, T., and R. Rotunno, 2003: The effects of subgrid model mixing and numerical filtering in simulations of mesoscale cloud systems. *Mon. Wea. Rev.*, **131**, 2085–2101, https://doi.org/10.1175/1520-0493(2003)131<2085:TEOSMM>2.0.CO;2.

Tang, S. L., and D. J. Kirshbaum, 2020: On the sensitivity of deep-convection initiation to horizontal grid resolution. *Quart. J. Roy. Meteor. Soc.*, **146**, 1085–1105, https://doi.org/10.1002/qj.3726.

Trier, S. B., W. C. Skamarock, M. A. LeMone, D. B. Parsons, and D. P. Jorgensen, 1996: Structure and evolution of the 22 February 1993 TOGA COARE squall line: Numerical simulations. *J. Atmos. Sci.*, **53**, 2861–2886, https://doi.org/10.1175/1520-0469(1996)053<2861:SAEOTF>2.0.CO;2.

Verrelle, A., D. Ricard, and C. Lac, 2017: Evaluation and improvement of turbulence parameterization inside deep convective clouds at kilometer-scale resolution. *Mon. Wea. Rev.*, **145**, 3947–3967, https://doi.org/10.1175/MWR-D-16-0404.1.

Warner, T. T., and H.-M. Hsu, 2000: Nested-model simulation of moist convection: The impact of coarse-grid parameterized convection on fine-grid resolved convection. *Mon. Wea. Rev.*, **128**, 2211–2231, https://doi.org/10.1175/1520-0493(2000)128<2211:NMSOMC>2.0.CO;2.

Weisman, M. L., and J. B. Klemp, 1982: The dependence of numerically simulated convective storms on vertical wind shear and buoyancy. *Mon. Wea. Rev.*, **110**, 504–520, https://doi.org/10.1175/1520-0493(1982)110<0504:TDONSC>2.0.CO;2.

——, and R. Rotunno, 2004: "A theory for strong long-lived squall lines" revisited. *J. Atmos. Sci.*, **61**, 361–382, https://doi.org/10.1175/1520-0469(2004)061<0361:ATFSLS>2.0.CO;2.

——, J. B. Klemp, and R. Rotunno, 1988: Structure and evolution of numerically simulated squall lines. *J. Atmos. Sci.*, **45**, 1990–2013, https://doi.org/10.1175/1520-0469(1988)045<1990:SAEONS>2.0.CO;2.

——, W. C. Skamarock, and J. B. Klemp, 1997: The resolution dependence of explicitly modeled convective systems. *Mon. Wea. Rev.*, **125**, 527–548, https://doi.org/10.1175/1520-0493(1997)125<0527:TRDOEM>2.0.CO;2.

Wyngaard, J. C., 2004: Toward numerical modeling in the "terra incognita". *J. Atmos. Sci.*, **61**, 1816–1826, https://doi.org/10.1175/1520-0469(2004)061<1816:TNMITT>2.0.CO;2.

Xue, M., K. K. Droegemeier, and V. Wong, 2000: The Advanced Regional Prediction System (ARPS)—A multi-scale nonhydrostatic atmospheric simulation and prediction model. Part I: Model dynamics and verification. *Meteor. Atmos. Phys.*, **75**, 161–193, https://doi.org/10.1007/s007030070003.

——, and Coauthors, 2001: The Advanced Regional Prediction System (ARPS)—A multi-scale nonhydrostatic atmospheric simulation and prediction tool. Part II: Model physics and applications. *Meteor. Atmos. Phys.*, **76**, 143–165, https://doi.org/10.1007/s007030170027.

——, D. Wang, J. Gao, K. Brewster, and K. K. Droegemeier, 2003: The Advanced Regional Prediction System (ARPS), storm-scale numerical weather prediction and data assimilation. *Meteor. Atmos. Phys.*, **82**, 139–170, https://doi.org/10.1007/s00703-001-0595-6.

——, F. Kong, K. W. Thomas, J. Gao, Y. Wang, K. Brewster, and K. K. Droegemeier, 2013: Prediction of convective storms at convection-resolving 1 km resolution over continental United States with radar data assimilation: An example case of 26 May 2008 and precipitation forecasts from spring 2009. *Adv. Meteor.*, **2013**, 259052, https://doi.org/10.1155/2013/259052.

Ye, G., X. Zhang, and H. Yu, 2023: Modifications to three-dimensional turbulence parameterization for tropical cyclone simulation at convection-permitting resolution. *J. Adv. Model. Earth Syst.*, **15**, e2022MS003530, https://doi.org/10.1029/2022MS003530.

Zalesak, S. T., 1979: Fully multidimensional flux-corrected transport algorithms for fluids. *J. Comput. Phys.*, **31**, 335–362, https://doi.org/10.1016/0021-9991(79)90051-2.

Zhang, J. A., F. D. Marks, J. A. Sippel, R. F. Rogers, X. Zhang, S. G. Gopalakrishnan, Z. Zhang, and V. Tallapragada, 2018: Evaluating the impact of improvement in the horizontal diffusion parameterization on hurricane prediction in the operational Hurricane Weather Research and Forecast (HWRF) model. *Wea. Forecasting*, **33**, 317–329, https://doi.org/10.1175/WAF-D-17-0097.1.

Zhang, X., B. Zhou, and F. Ping, 2021: Effects of subgrid-scale horizontal turbulent mixing on a simulated convective storm at kilometer-scale resolutions. *Atmos. Res.*, **254**, 105445, https://doi.org/10.1016/j.atmosres.2020.105445.

Zhou, B., J. S. Simon, and F. K. Chow, 2014: The convective boundary layer in the terra incognita. *J. Atmos. Sci.*, **71**, 2545–2563, https://doi.org/10.1175/JAS-D-13-0356.1.

——, S. Sun, K. Yao, and K. Zhu, 2018: Reexamining the gradient and countergradient representation of the local and nonlocal heat fluxes in the convective boundary layer. *J. Atmos. Sci.*, **75**, 2317–2336, https://doi.org/10.1175/JAS-D-17-0198.1.

Zhu, K., and Coauthors, 2018: Evaluation of real-time convection-permitting precipitation forecasts in China during the 2013–2014 summer season. *J. Geophys. Res. Atmos.*, **123**, 1037–1064, https://doi.org/10.1002/2017JD027445.